Satellite Products and Services Review Board

VOLCAT Algorithm Theoretical Basis Document

Compiled by the
SPSRB Common Standards Working Group

Version 1.0
January, 2025

VOLCAT: ALGORITHM THEORETICAL BASIS DOCUMENT VERSION 1.0

AUTHORS:

Mike Pavolonis (NOAA NESDIS)

Justin Sieglaff (UW-Madison; CIMSS)

Ray Garcia (UW-Madison; CIMSS)

Corey Calvert (UW-Madison; CIMSS)

DOCUMENT HISTORY
DOCUMENT REVISION LOG

The Document Revision Log identifies the series of revisions to this document since the baseline release. Please refer to the above page for version number information.

DOCUMENT TITLE: Algorithm Theoretical Basis Document Template			
DOCUMENT CHANGE HISTORY			
Revision No.	**Date**	**Revision Originator Project Group**	**CCR Approval # and Date**
1.0	January 2025	Initial Version	N/A

LIST OF CHANGES

Significant alterations made to this document are annotated in the List of Changes table.

DOCUMENT TITLE: Algorithm Theoretical Basis Document Template					
LIST OF CHANGE-AFFECTED PAGES/SECTIONS/APPENDICES					
Version Number	**Date**	**Changed By**	**Page**	**Section**	**Description of Change(s)**

TABLE OF CONTENTS

LIST OF TABLES AND FIGURES

Page

Figures

Tables

1 INTRODUCTION

1.1 Product Overview

1.1.1 Product Description

The **VOL**canic **C**loud **A**nalysis **T**oolkit (or VOLCAT) is an artificial intelligence application suite that utilizes satellite observations (and other datasets) to automatically detect, characterize, and track volcanic clouds and hazards during the entire life cycle of a volcanic emission. The VOLCAT products provide essential information to end-users with the responsibility of protecting life and property related to volcanic hazards—the most significant impact is the aviation sector, as jet engines can be damaged and even fail when ingesting volcanic ash. The VOLCAT information is also essential for the prediction of volcanic clouds and hazards through the assimilation into dispersion forecast models (e.g., NOAA HYSPLIT model). The VOLCAT system alerts end-users of newly emergent volcanic clouds with minimal latency. The VOLCAT system tracks the volcanic clouds, providing estimates of cloud top height and column mass loading through the volcanic cloud lifecycle. The final output of the VOLCAT system are event-based files, not traditional 2-D fields that correspond to the input satellite observation size. Events are defined as discrete volcanic emissions as detected by VOLCAT and automatically assigned to a source volcano as determined by the VOLCAT system. The output is organized by volcano and satellite sensor. A volcano may have more than one event being tracked by the VOLCAT system at any time and data describing each event is contained in output files for each volcano and satellite sensor combination. The unique, event-driven output format is unique relative to the majority of satellite-based products, and more details about the output format is included in this document.

Volcanic clouds impact a variety of societal-economic sectors, but most directly the aviation sector, where aircraft encounters with volcanic hazards can pose significant immediate safety situations (e.g., aircraft engine failure when exposed to large amounts of volcanic ash) to long-term safety and economic concerns due to gradual equipment damage due to volcanic ash exposure. The aviation industry, following the International Civil Aviation Organization (ICAO) guidelines, historically avoids all areas of known volcanic ash and has a stated the goal of 5-minute latency or better for notification of newly emergent volcanic hazards. Within the coming decade, based on new research, the ICAO guidelines are shifting from complete avoidance to a risk-managed, probabilistic approach, where low concentrations of volcanic ash can be transversed by aircraft. The VOLCAT products are essential to meet the new ICAO guidelines and have a long history of real-time experimental usage by end-users. The end-users with primary responsibility for aviation safety include Volcanic Ash Advisory Centers (VAACs) (there are 9 VAACs across the globe, each with a region of responsibility), volcano observatories, and other partners.

1.1.2 Product Requirements

There are a number of different types of requirements regarding volcanic hazards with respect to aviation safety. The requirement types include automated eruption detection, eruption alerting, automated ash cloud tracking, ash properties and uncertainty, automated SO_2 cloud tracking, SO_2 properties and uncertainty, eruption source parameters, and model tools. The VOLCAT requirements are fully documented in the VOLCAT CDR slides—ATB supplemental.

1.2 Satellite Instrument Description

VOLCAT requires multi-spectral GEO or LEO satellite imager observations. VOLCAT is designed to operate with the current global constellation of GEO and LEO meteorological satellite imagers, utilizing as many pertinent satellite channels as offered by each sensor. The VOLCAT system will operate with the following satellite imagers: GOES ABI, Himawari AHI, Meteosat Third Generation FCI, Meteosat Second Generation SEVIRI, VIIRS, Metop-AVHRR. Full details on which spectral channels as a function of satellite instrument are included later in this document.

The VOLCAT operational transition plan established work to occur in 3 stages. The first stage (Stage 1) is in progress as of the writing of this document. The VOLCAT Stage 1 operational transition will produce VOLCAT ash products for many GEO and LEO satellites. The Stage 2 and Stage 3 transitions will include added capabilities, support for new sensors, and incorporation of improvements from current research efforts.

VOLCAT is also capable of detection and characterizing sulfur dioxide (SO_2). Given the narrow absorption lines in the infrared (IR) portion of the electromagnetic spectrum owing to SO_2, high-spectral resolution infrared sounder data is also necessary for VOLCAT SO_2 detection and characterization. The VOLCAT SO_2 detection and characterization will be part of the Stage 2 operational transition (following successful operational transition of Stage 1) and further SO_2 details will be added at that time. It should be noted high-spectral resolution IR sounders supported by the VOLCAT include CrIS, current research is adding support for IASI and IASI-NG.

2 ALGORITHM DESCRIPTION

2.1 Processing Outline

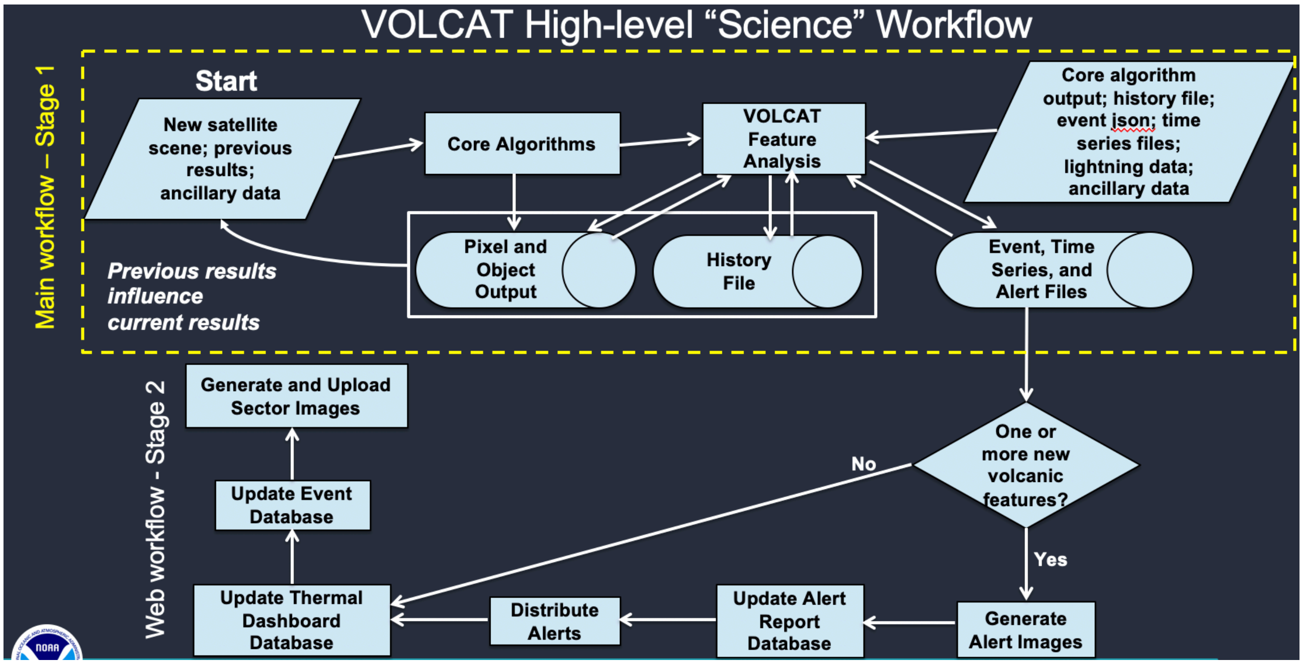

Figure 2- 1 Illustration of the VOLCAT workflow. Satellite observations trigger processing containers, ingesting satellite data for current observation as well as VOLCAT state inputs (e.g., VOLCAT history, previous VOLCAT intermediate output). The final end-user provided outputs include VOLCAT Event netcdf files and VOLCAT Event json files. VOLCAT Stage 2 will include additional output in the form of database entries, alert imagery, which feed the VOLCAT website, which is the primary end-user uptake of VOLCAT information.

Figure 2- 1 demonstrates a high-level summary of the VOLCAT processing flow. The VOLCAT application suite is a combination of compiled Fortran and C executable code and a high-level python wrapper. The VOLCAT Fortran processing code is a two-step process. The first step performs satellite data ingest, calibration, navigation as well as ingest of previous VOLCAT results. The first step of VOLCAT Fortran code then computes all necessary metrics to detect and characterize volcanic clouds contained within the satellite observations. The second step of the VOLCAT Fortran code ingests intermediate output from the first step to perform volcanic cloud tracking, quality control, and alerting. Upon conclusion of the two Fortran steps, python functionality ingests VOLCAT intermediate output to generate final output, which are VOLCAT event files and VOLCAT event JSON files. The unique, event-centric output format/concept of the VOLCAT system is further described in section 2.4.

2.2 Algorithm Input

2.2.1 Satellite Inputs

The satellite data inputs consist of reflectance factors, brightness temperatures, geolocation information, and various satellite and solar viewing geometry information. These inputs are formatted differently for each satellite instrument and the VOLCAT system is equipped to ingest these file types for each of the supported satellite instruments. Figure 2- 2 shows the satellites and instruments supported by VOLCAT.

Present Day Satellites within NCCF

Satellite(s)	Instrument(s)	Nadir Resolution of VOLCAT Output
GOES-East, GOES-West	ABI, GLM	2 km
Himawari-8, Himawari-9	AHI	2 km
Metop-B, Metop-C	AVHRR, IASI*	1 km
MTG-I1	FCI, LI	2 km
MSG	SEVIRI	3 km
SNPP	VIIRS, CrIS*	750 m
NOAA-20, NOAA-21	VIIRS, CrIS*	750 m

All present day sensors will be implemented in Stage 1, except IASI and CrIS, which will be added in Stage 2

Upcoming Satellites within NCCF

Satellite(s)	Instrument(s)	Nadir Resolution of VOLCAT Output
MTG-I1	FCI, LI	2 km
Metop-SG A1	METimage, IASI-NG	500 m

These satellites will be added in Stage 2 or 3 (depends on program schedules)

Figure 2- 2 Current day satellites and sensors supported by VOLCAT processing system.

Additionally, the VOLCAT system is designed to utilize and ingest pertinent satellite channels useful for the detection and characterization of volcanic clouds as a function of satellite instrument. Figure 2- 3 provides details of which satellite channels are ingested as function of satellite/sensor (note in addition to ABI channels, for GOES, GLM L2 data are also ingested).

Default Satellite Input

Satellite(s)	Sensor(s)	Default Inputs
GOES-East GOES-West	ABI GLM	0.64, 3.9, 7.0, 7.4, 8.5, 10.3, 11.2, 12.3, 13.3 µm GLM L2
Himawari-8 Himawari-9	AHI	0.64, 3.9, 7.0, 7.4, 8.5, 10.3, 11.2, 12.3, 13.3 µm
MTG-I1	FCI	0.64, 3.8, 6.3, 7.35, 8.70, 10.5, 12.3, 13.3 µm
MSG	SEVIRI	0.635, 3.92, 6.25, 7.35, 8.7, 10.8, 12.0, 13.4 µm
SNPP NOAA-20, NOAA-21	VIIRS CrIS*	0.672, 3.7, 4.05, 8.55, 10.763, 12.013 µm MW and LW bands
Metop-B Metop-C	AVHRR IASI*	0.63, 3.74, 10.8, 12.0 µm MW and LW bands

Every algorithm module: is sensor agnostic, allows for many different channel combinations, and includes graceful degradation (where possible) when bad L1b data are encountered

Figure 2- 3 Satellite channels and other satellite data ingested by VOLCAT as a function of satellite. CrIS and IASI are needed for VOLCAT SO_2 processing and will be included as part of the Stage 2 operational transition and may be utilized in the future by the VOLCAT ash processing pending future research.

2.2.2 Ancillary Inputs

The VOLCAT system requires ingest of both static and dynamic ancillary files necessary to successfully process data. The static ancillary data includes a variety of inputs, including configuration files, look-up tables for machine learning and associated constants, ash property retrieval coefficients and associated constants, and Global Volcanism Program volcano and feature selection thresholds. The dynamic ancillary data include GFS 12 hour forecasts, global snow mask, and global SST composite. Complete static ancillary file listing and brief descriptions can be found in the VOLCAT CDR slides.

2.2.3 Forward Model

The VOLCAT processing system has self-contained forward radiative transfer model that computes clear-sky brightness temperatures, which are used by the VOLCAT algorithms. The forward model contains static ancillary data described in the link provided in the previous subsection.

2.3 Theoretical Description

2.3.1 Physical Description

The VOLCAT system is an application suite that fuses a number of components designed to detect, characterize, and track volcanic clouds through their complete life-cycle—from monitoring thermal activity at volcano vents prior to volcanic eruptions, to emission at volcanic vents, to dissipation. Volcanic eruptions span many orders of magnitude in the amount of material injected into the atmosphere (Newhall and Self, 1982) and the residence time in the atmosphere varies substantially, with significant impact related to particle size distribution of emitted material and meteorological conditions. This section is intended to briefly describe each component of the VOLCAT application suite and how these components are integrated to meet user requirements through the entire life cycle of volcanic emissions.

VOLCAT monitors thermal activity at volcano vents with an algorithm that utilizes multi-spectral observations to detect heat sources co-located with known volcano locations and computes volcanic radiative power utilizing observations near 3.9 μm. The monitoring of thermal activity impacts downstream volcanic cloud detection algorithms as an increase in thermal activity often precedes volcanic eruptions. There are two primary methods for volcanic cloud detection within VOLCAT, one is a multi-spectral ash signature detection methodology (Pavolonis et al., 2015a,b), which is applied to both geostationary and low-earth orbit observations and an explosive eruptive cloud detection methodology which relies on cloud growth anomaly metrics from frequent geostationary observations (Pavolonis et al., 2018). The cloud growth anomaly detection algorithm is necessary to detect explosive volcanic eruptions where considerable amounts of water and ice particles effectively mask the multi-spectral signature of the ash particles. For all detected volcanic clouds, the physical properties of the volcanic clouds are characterized using a physical IR retrieval algorithm which provides estimates of volcanic cloud top height, total column ash mass loading, and cloud particle effective radius (Pavolonis et al., 2013). The detection and characterization algorithm results, along with the multispectral reflectance and brightness temperature observations, are input into a volcanic cloud tracking algorithm. This algorithm utilizes a multi-spectral kd-tree for tracking volcanic clouds between each satellite observation, which is needed to fully monitor the complete life cycle of volcanic clouds (e.g., from emission to dissipation).

The VOLCAT ash detection methodology exploits differential absorption characteristics of volcanic ash particles relative to water and ice cloud particles across the visible, near IR and thermal IR portions of the electromagnetic spectrum (Figure 2- 4).

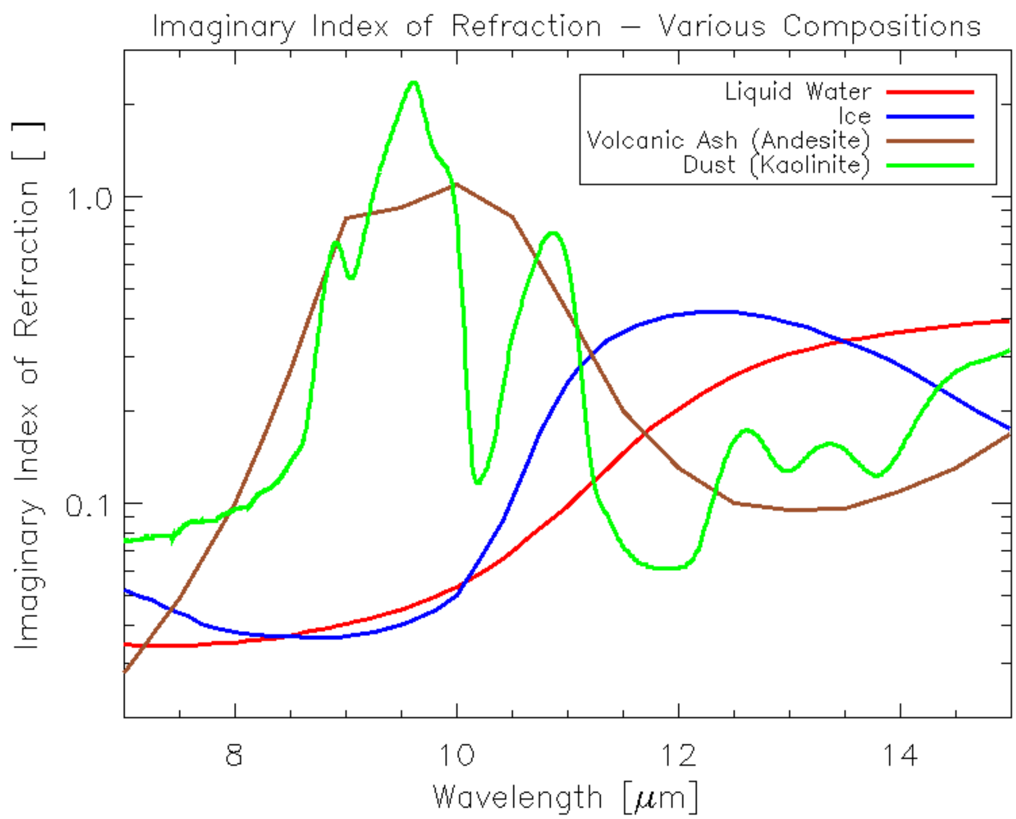

Figure 2- 4 The imaginary index of refraction for liquid water (red), ice (blue), andesite (brown), and kaolinite (green) is shown as a function of wavelength.

The exploitation of differing absorption characteristics to detect volcanic ash clouds and associated spatial metrics used is fully documented in Pavolonis et al., 2015a,b.

2.3.2 Mathematical Description

The mathematical section of this document focuses on the ash cloud retrieval properties, as these quantities are the most fundamental to end-users. The VOLCAT ash retrieval algorithm utilizes either 3 or 2 long-wave IR channels depending on the satellite sensor. For example, GOES ABI channels 14, 15, and 16 (11 μm, 12 μm, and 13.3 μm) are used and for VIIRS channels, 15 and 16 (11 and 12 μm)) are used; channels utilized by satellite sensor can further be found in Pavolonis et al., 2015a,b and Pavolonis et al., 2013. These channels are referred to by their approximate central wavelengths (11 μm, 12 μm, and 13.3 μm) throughout this section. The algorithm does not directly retrieve ash height or ash mass loading. It retrieves ash cloud effective temperature, effective emissivity, and a microphysical parameter. These retrieved parameters are then used to estimate the ash cloud height and mass loading.

2.3.2.1 Cloudy Radiative Transfer

Assuming a satellite viewing perspective (e.g. upwelling radiation), a fully cloudy field of view, a non-scattering atmosphere (no molecular scattering), and a negligible contribution from downwelling cloud emission or molecular emission that is reflected by the surface and transmitted to the top of troposphere (Zhang and Menzel (2002) showed that this term is very small at infrared wavelengths), the cloudy radiative transfer equation for a given infrared channel or wavelength can be written as in Equation 1 (e.g. Heidinger and Pavolonis, 2009).

$$R_{obs}(\lambda) = \varepsilon(\lambda)R_{ac}(\lambda) + t_{ac}(\lambda)\varepsilon(\lambda)B(\lambda, T_{eff}) + R_{clr}(\lambda)(1-\varepsilon(\lambda)) \quad \text{(Eq. 1)}$$

In Equation 1, λ is wavelength, R_{obs} is the observed radiance, R_{clr} is the clear sky radiance. R_{ac} and t_{ac} are the above cloud upwelling atmospheric radiance and transmittance, respectively. B is the Planck Function, and T_{eff} is the effective cloud temperature. The effective cloud emissivity (Cox, 1976) is given by ε. To avoid using additional symbols, the angular dependence is simply implied. While the above radiative transfer equation is simple in that it does not explicitly account for cloud scattering (cloud scattering is implicitly accounted for in the effective emissivity, see Cox, 1976) and that the cloud can be treated as a single layer, it does allow for semi-analytic derivations of the observations to the controlling parameters (i.e. cloud temperature). This is critical because it allows for an efficient retrieval without the need for large lookup tables.

Equation 1 can readily be solved for the effective cloud emissivity as follows:

$$\varepsilon(\lambda) = \frac{R_{obs}(\lambda) - R_{clr}(\lambda)}{[B(\lambda, T_{eff})t_{ac}(\lambda) + R_{ac}(\lambda)] - R_{clr}(\lambda)} \quad \text{(Eq. 2)}$$

In Equation 2, the term in brackets in the denominator is the blackbody cloud radiance that is transmitted to the top of atmosphere (TOA) plus the above cloud (ac) atmospheric radiance. This term is dependent upon the cloud vertical location.

In this retrieval algorithm, the effective cloud emissivity is allowed to vary spectrally. It is the spectral variation of the effective cloud emissivity that holds the cloud microphysical information (particle size, shape, and composition), which is important for calculating the ash mass loading. To account for this spectral variation, the effective cloud emissivity is used to calculate effective absorption optical depth ratios; otherwise known as β-ratios (see Inoue 1987; Parol et al., 1991; Giraud et al., 1997; and Heidinger and Pavolonis, 2009). For a given pair of spectral cloud emissivities ($\varepsilon(\lambda_1)$ and $\varepsilon(\lambda_2)$):

$$\beta_{obs} = \frac{\ln[1-\varepsilon(\lambda_1)]}{\ln[1-\varepsilon(\lambda_2)]} = \frac{\tau_{abs}(\lambda_1)}{\tau_{abs}(\lambda_2)} \quad \text{(Eq. 3)}$$

Notice that Equation 3 can simply be interpreted as the ratio of effective absorption optical depth (τ) at two different wavelengths or channels. Allowing the ash cloud microphysics to vary will also allow for improved estimates of ash cloud height as well.

An appealing quality of β_{obs}, is that it can be interpreted in terms of the single scatter properties, which can be computed for a given cloud composition and particle distribution. Following Van de Hulst (1980) and Parol et al. (1991), a spectral ratio of scaled extinction coefficients can be calculated from the single scatter properties (single scatter albedo, asymmetry parameter, and extinction cross section), as follows.

$$\beta_{theo} = \frac{[1.0-\omega(\lambda_1)g(\lambda_1)]\sigma_{ext}(\lambda_1)}{[1.0-\omega(\lambda_2)g(\lambda_2)]\sigma_{ext}(\lambda_2)} \quad \text{(Eq. 4)}$$

In Equation 4, β_{theo} is the spectral ratio of scaled extinction coefficients, ω is the single scatter albedo, g is the asymmetry parameter, and σ_{ext} is the extinction cross section. At wavelengths in the 8 – 15 μm range, where multiple scattering effects are small, β_{theo}, captures the essence of the cloudy radiative transfer such that,

$$\beta_{obs} \approx \beta_{theo} \quad \text{(Eq. 5)}$$

Equation 5, which was first shown to be accurate for observation in the 10 – 12 μm "window" by Parol et al. (1991), only depends upon the single scatter properties. This relationship is also verified in Pavolonis (2010).

2.3.2.2 Microphysical Relationships

Since the ash retrieval utilizes three channels (for applicable sensors), two different β_{obs} are required to describe the spectral variation of cloud emissivity. Unfortunately, imager measurements do not contain enough information to retrieve more than one β_{obs}, so a pre-established relationship between the two β_{obs} must be used to constrain the retrieval problem. More specifically, the ash composition (e.g. the type of rock) and the ash particle habit (e.g. shape) must be assumed. This constraint, however, does not prevent the retrieval of quality ash particle size information. This pre-established relationship is derived from the corresponding spectral ratio of scaled extinction coefficients, as defined by Equation 4. All of the necessary microphysical assumptions are described below.

The volcanic ash particles are taken to be composed of andesite (Pollack et al, 1973). The size distribution was assumed to be lognormal. Lognormal distributions of andesite have been commonly used to model volcanic ash (e.g. Wen and Rose, 1994; Pavolonis et al., 2006; Prata and Grant, 2001). The andesite particles were assumed to be spherical and Mie theory is used to compute the single scatter properties. Of course, real volcanic ash particles actually take on a variety of irregular shapes that are very difficult to model, and the ash composition (e.g. the type of rock) varies from volcano to volcano. Fortunately, the sensitivity to particle habit and composition in the infrared is much smaller than the sensitivity to particle size (Wen and Rose, 1994). Given the composition and habit assumptions, the needed β relationship can be computed from the Mie generated single scatter properties. Figure 2- 5 below shows the variation of the 11 and 12 μm β with the 11 and 13.3 μm β computed using Equation 4, where the 11 μm channel is always placed in the denominator of Equation 4. Hereafter, these β's are referred to as β(12/11μm) and β(13.3/11μm), respectively. In the retrieval, β(12/11μm) is a free parameter and β(13.3/11μm) is determined using the empirical relationship shown in Figure 2- 5. The form of the empirical relationship is as follows.

$$\beta(13.3/11\mu m) = c4[\beta(12/11\mu m)]^4 + c3[\beta(12/11\mu m)]^3 + c2[\beta(12/11\mu m)]^2 + c1[\beta(12/11\mu m)] + c0$$
(Eq. 6)

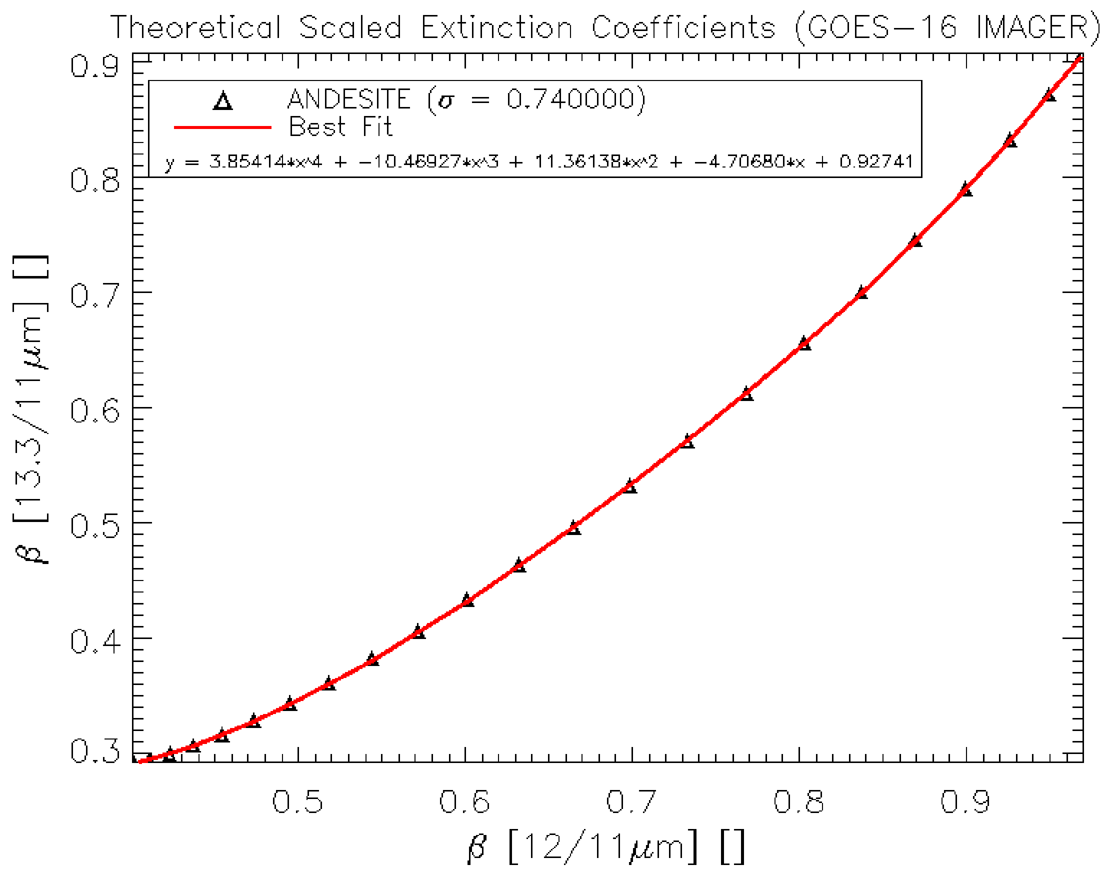

Figure 2- 5 The 13.3/11 μm scaled extinction ratio (β(13.3/11 μm)) is shown as a function of the 12/11 μm scaled extinction ratio (β(12/11 μm)) for andesite spheres (volcanic ash). The andesite effective particle radius was varied from 1 to 13 μm, where larger values of β indicate larger particles. These β's were derived from single scatter properties calculated using Mie Theory and integrated over the corresponding ABI spectral response functions. The red line is the fourth degree polynomial fit.

Additional single scatter property based microphysical relationships are needed to convert the retrieved β(12/11μm) to an effective particle radius (r_{eff}) and the 11-μm extinction cross section (σ_{ext}(11μm)). Both of these parameters are needed when estimating the ash mass loading. Figure 2- 6 and Figure 2- 7 show the relationship used to convert the retrieved β(12/11μm) to an effective particle radius and extinction coefficient, respectively. The forms of these empirical relationships are as follows.

$$r_{eff} = \exp(c4[\beta(12/11\mu m)]^4 + c3[\beta(12/11\mu m)]^3 + c2[\beta(12/11\mu m)]^2 + c1[\beta(12/11\mu m)] + c0)$$
(Eq. 7)

$$\sigma_{ext}(11\mu m) = \exp(c4[\beta(12/11\mu m)]^4 + c3[\beta(12/11\mu m)]^3 + c2[\beta(12/11\mu m)]^2 + c1[\beta(12/11\mu m)] + c0)$$ (Eq. 8)

For notational convenience, generic symbols are used for the regression coefficients, which actually differ between Equations 6 - 8.

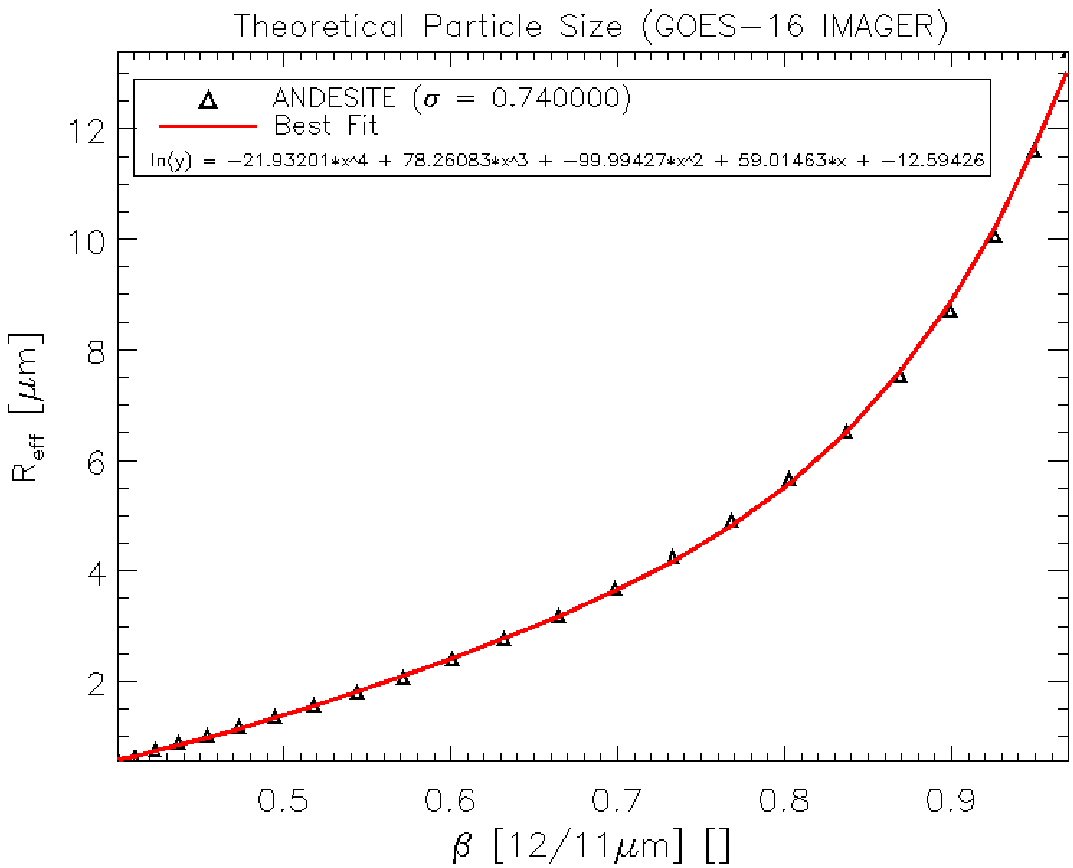

Figure 2- 6 The effective particle radius is shown as a function of the 12/11 μm scaled extinction ratio (β(12/11 μm)) for andesite spheres (volcanic ash). The β(12/11 μm) was derived from single scatter properties calculated using Mie Theory and integrated over the corresponding ABI spectral response functions. The red line is the fourth degree polynomial fit.

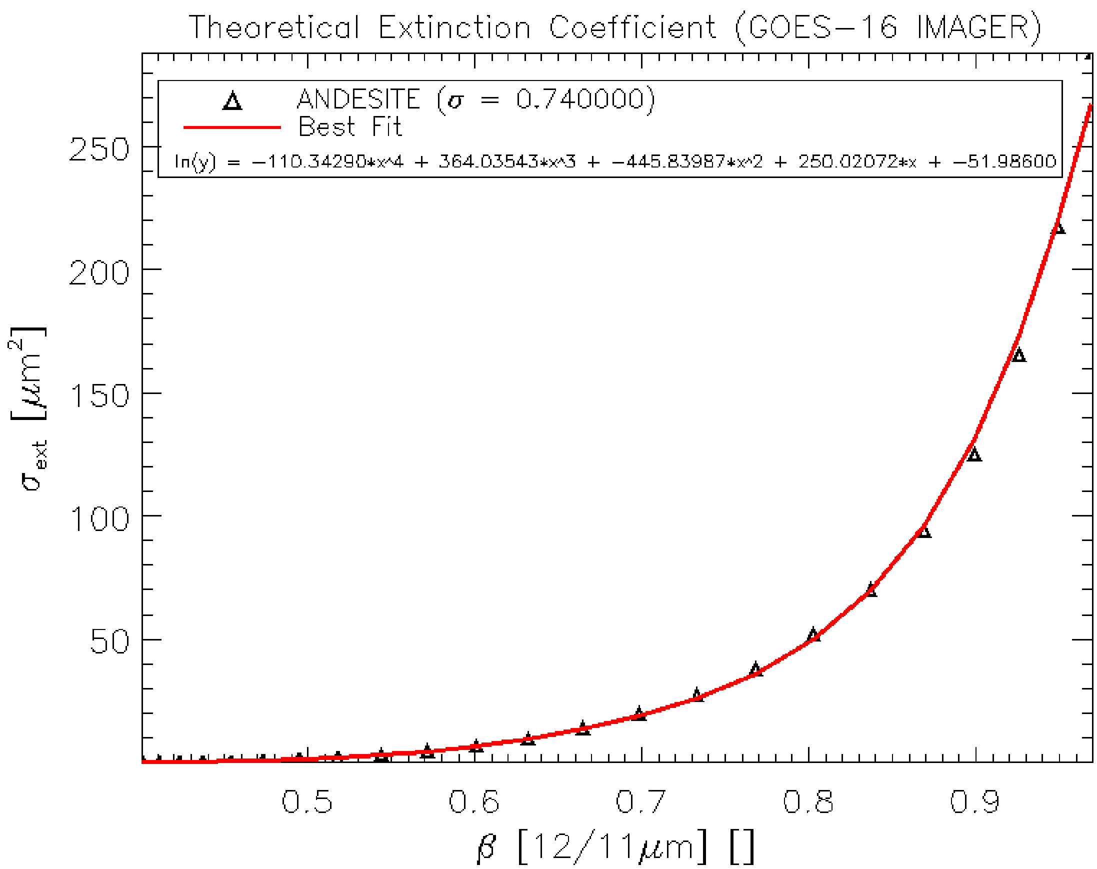

Figure 2- 7 The extinction cross section is shown as a function of the 12/11 μm scaled extinction ratio (β(12/11 μm)) for andesite spheres (volcanic ash). The β(12/11 μm) was derived from single scatter properties calculated using Mie Theory and integrated over the corresponding ABI spectral response functions. The red line is the fourth degree polynomial fit.

Given the more limited spectral channels available from some sensors (e.g., VIIRS, Metop-AVHRR), the physical retrieval is reduced to 2-channels. The retrieved parameters still include ash cloud effective temperature, effective emissivity, and a microphysical parameter. These retrieved parameters are then used to estimate the ash cloud height and mass loading. The microphysical relationships described by Equations 7 and 8 are shown in Figure 2- 8 and Figure 2- 9, respectively. These figures show the relationship used to convert the retrieved β(12/11μm) to an effective particle radius and extinction coefficient, respectively. For notational convenience, generic symbols are used for the regression coefficients, which actually differ between Equations 7 and 8.

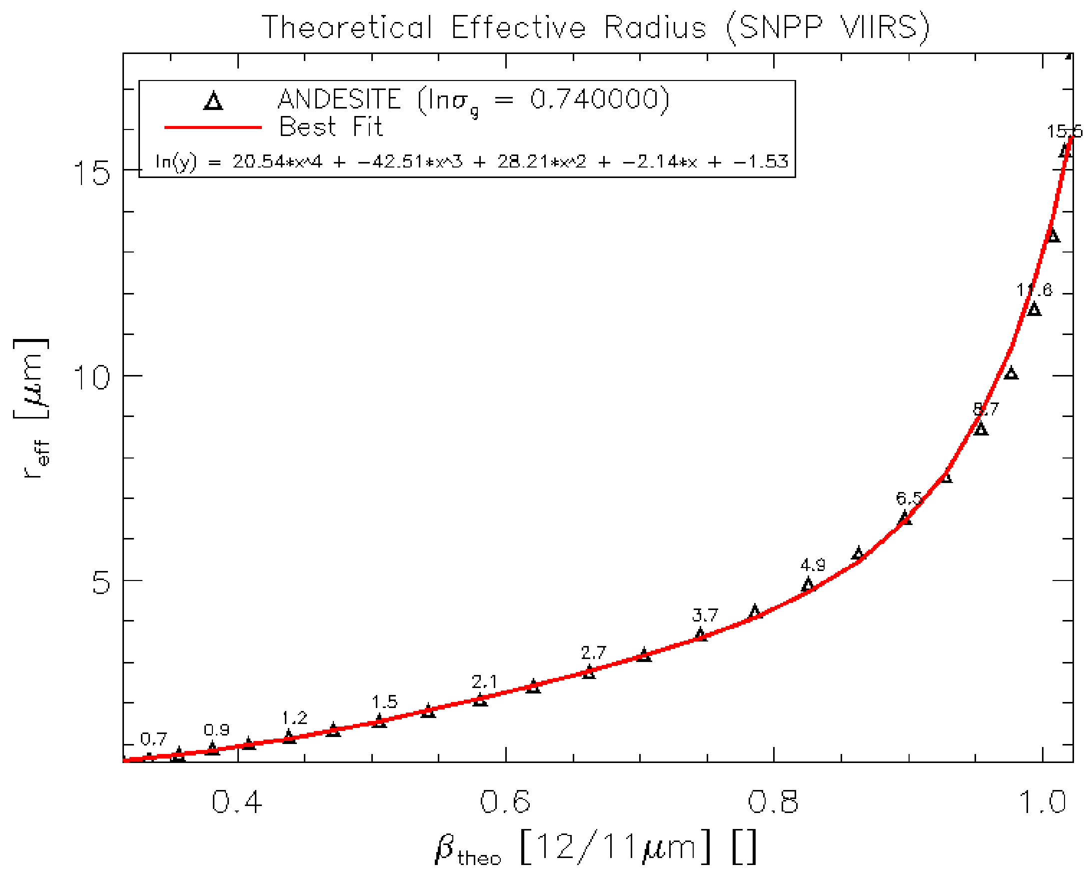

Figure 2- 8 The effective particle radius is shown as a function of the 12/11 μm scaled extinction ratio (β(12/11 μm)) for andesite spheres (volcanic ash). The β(12/11 μm) was derived from single scatter properties calculated using Mie Theory and integrated over the corresponding VIIRS spectral response functions. The red line is the fourth degree polynomial fit.

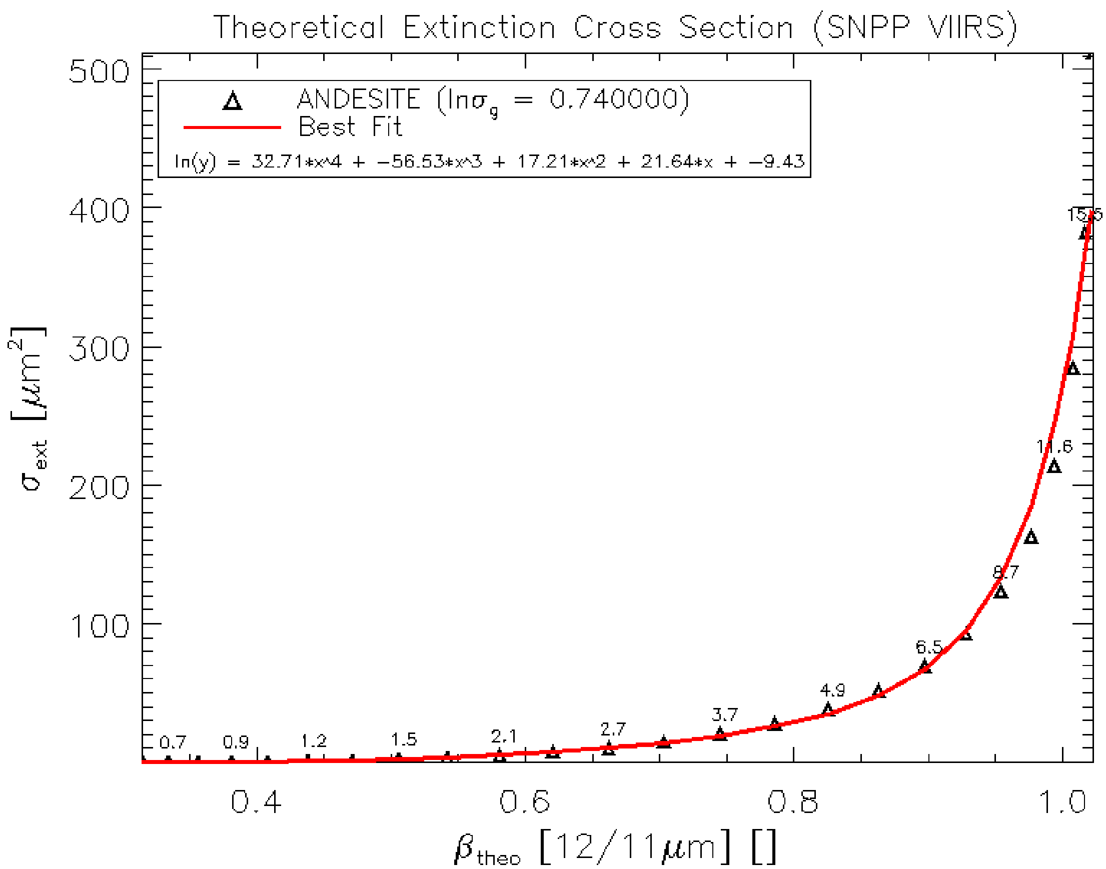

Figure 2- 9 The extinction cross section is shown as a function of the 12/11 μm scaled extinction ratio (β(12/11 μm)) for andesite spheres (volcanic ash). The β(12/11 μm) was derived from single scatter properties calculated using Mie Theory and integrated over the corresponding VIIRS spectral response functions. The red line is the fourth degree polynomial fit.

2.3.2.3 Physical Retrieval Mathematical Description

The mathematical approach employed here is the optimal estimation approach described by Rodgers (1976). The optimal estimation approach is also often referred to as a 1DVAR approach. The benefits of this approach are that it is flexible and allows for the easy addition or subtraction of new observations or retrieved parameters. Another benefit of this approach is that it generates automatic estimates of the retrieval errors. The optimal estimation approach minimizes a cost function, ϕ, given by

$$\phi = (x - x_a)^T S_a^{-1}(x - x_a) + (y - f(x))^T S_y^{-1}(y - f(x)) \quad \text{(Eq. 9)}$$

Where y is the vector of observations, x is the vector of retrieved parameters, f(x) represents the forward model, which is a function of x, and x_a is the *a priori* value of x. The matrices S_y and S_a are the error covariance matrices of the forward model and *a priori* values respectively. In our retrieval, the y, x, and x_a vectors are defined as follows.

$$y = \begin{pmatrix} BT(11\mu m) \\ BTD(11-12\mu m) \\ BTD(11-13.3\mu m) \end{pmatrix} \quad \text{(Eq. 10a)} \qquad x = \begin{pmatrix} T_{eff} \\ \varepsilon(11\mu m) \\ \beta(12/11\mu m) \end{pmatrix} \quad \text{(Eq. 10b)} \qquad x_a = \begin{pmatrix} T_{eff}\_ap \\ \varepsilon(11\mu m)\_ap \\ \beta(12/11\mu m)\_ap \end{pmatrix} \quad \text{(Eq. 10c)}$$

The observation vector, y, consists of the 11 μm brightness temperature (BT), the 11 minus 12 μm brightness temperature difference (BTD) and the 11 – 13.3 μm BTD *(3-channel retrieval only)*. The use of BTD's is needed to capture the cloud microphysical signal. The retrieved parameters, x, are the effective cloud temperature (T_{eff}), the 11 μm cloud emissivity (ε(11μm)), and the 12/11 μm effective absorption optical depth ratio (β(12/11μm)). The symbols for the first guess or *a priori* estimates of the retrieved parameters are appended with "_ap." As explained earlier, these retrieved parameters are then used to estimate the ash cloud height and mass loading. The ash height and mass loading cannot be retrieved directly because they are not variables in the cloudy infrared radiative transfer equation.

2.3.2.4 Determining the a priori Values and Associated Uncertainty

The *a priori* values and their associated uncertainties act to constrain the retrieved parameters when the measurements contain little or no information on one or more of the retrieved parameters. The *a priori* error covariance matrix (Equation 11) is assumed to be diagonal (e.g. errors in the first guess of each parameter are uncorrelated). The *a priori* values and their uncertainties depend on whether the ash cloud overlaps a lower meteorological cloud or if it is single layered, as determined by the volcanic ash detection routine. Table 2- 1 shows the *a priori* values and their estimated uncertainties for both single and multilayered conditions. When forming the matrix given by Equation 11, the values in Table 2- 1 need to be squared. These values were largely determined through analysis of semi-transparent ice clouds observed by spaceborne lidar (e.g. Heidinger and Pavolonis, 2009). Thus, these *a priori* estimates may not be ideal for volcanic ash clouds, but lidar observations of ash clouds are very rare, so better estimates are difficult to make. A large uncertainty is assigned to each *a priori* parameter, so that the measurements are given a high weight during the iteration. In summary, these values will likely be adjusted as more unique observations (e.g. lidar, in-situ, etc…) of volcanic ash clouds become available.

$$S_a = \begin{pmatrix} \sigma^2_{Teff\_ap} & 0.0 & 0.0 \\ 0.0 & \sigma^2_{\varepsilon(11\mu m)\_ap} & 0.0 \\ 0.0 & 0.0 & \sigma^2_{\beta(12/11\mu m)\_ap} \end{pmatrix} \quad \text{(Eq. 11)}$$

Table 2- 1 The a priori (first guess) retrieval values used in the 3-channel volcanic ash retrieval. The T_{eff} first guess is a function of the 11 μm brightness temperature, B(11μm). The ε(11μm) first guess is a function of the satellite zenith angle, θ_{sat}.

Parameter	**Single Layer *a priori***	**Single Layer *a priori* Uncertainty**	**Multi-layer *a priori***	**Multi-layer *a priori* Uncertainty**
σTeff_ap	BT(11μm) – 15 K	40 K	BT(11μm) – 15 K	40 K
σε(11μm)_ap	$1.0\text{-}e^{(-0.5/\cos(\theta_{sat}))}$	0.5	$1.0\text{-}e^{(-0.5/\cos(\theta_{sat}))}$	0.5
σβ(12/11μm)_ap	0.8	0.3	0.8	0.3

Table 2- 2 below shows reflects different *a priori* and uncertainty for the 2-channel retrieval for sensors like VIIRS.

Table 2- 2 The a priori (first guess) retrieval values used in the 2-channcel volcanic ash retrieval. The T_{eff} first guess is a function of the 11 μm brightness temperature, B(11μm). The ε(11μm) first guess is a function of the satellite zenith angle, θ_{sat}.

Parameter	**Single Layer *a priori***	**Single Layer *a priori* Uncertainty**	**Multi-layer *a priori***	**Multi-layer *a priori* Uncertainty**
σTeff_ap	BT(11μm) – 10 K	10 K	BT(11μm) – 5 K	10 K
σε(11μm)_ap	$1.0\text{-}e^{(-0.5/\cos(\theta_{sat}))}$	0.7	$1.0\text{-}e^{(-0.5/\cos(\theta_{sat}))}$	0.5
σβ(12/11μm)_ap	0.8	0.2	0.8	0.2

2.3.2.5 The Forward Model

For notational convenience, we define the "blackbody" top-of-atmosphere cloud radiance, $R_{cld}(\lambda)$, as follows. All other terms in this equation have been defined previously.

$$R_{cld}(\lambda) = R_{ac}(\lambda) + t_{ac}(\lambda)B(\lambda, T_{eff}) \quad \text{(Eq. 12)}$$

Based on Equations 1 and 12, the radiance for each channel used in the retrieval is given by Equations 13 – 15. The Planck Function is then used to convert the radiances to brightness temperature, from which brightness temperature differences can be constructed.

$$R_{obs}(11\mu m) = \varepsilon(11\mu m)R_{cld}(11\mu m) + R_{clr}(11\mu m)(1-\varepsilon(11\mu m))$$ (Eq. 13)

$$R_{obs}(12\mu m) = \varepsilon(12\mu m)R_{cld}(12\mu m) + R_{clr}(12\mu m)(1-\varepsilon(12\mu m))$$ (Eq. 14)

$$R_{obs}(13.3\mu m) = \varepsilon(13.3\mu m)R_{cld}(13.3\mu m) + R_{clr}(13.3\mu m)(1-\varepsilon(13.3\mu m))$$ (Eq. 15) *(3-channel retrieval only)*

The 12 and 13.3 μm cloud emissivities are not retrieved, so they must be determined at the beginning of each iteration in the optimal estimation scheme using ε(11μm), β(12/11μm), and Equation 6 (in the case of ε(13.3μm)) to evaluate the following relationships, which were derived from Equation 2.

$$\varepsilon(12\mu m) = 1 - [1-\varepsilon(11\mu m)]^{\beta(12/11\mu m)}$$ (Eq. 16)

$$\varepsilon(13.3\mu m) = 1 - [1-\varepsilon(11\mu m)]^{\beta(13.3/11\mu m)}$$ (Eq. 17) *(3-channel retrieval only)*

If the volcanic ash detection results indicate that an ash cloud likely overlaps a lower meteorological cloud, then the clear sky radiance, $R_{clr}(\lambda)$, in Equations 13 – 15 is replaced by the radiance from and above a black (emissivity = 1 at all wavelengths) elevated surface in an effort to account for the impact of the lower cloud layer.

The errors associated with the forward model, f(x), must be characterized and expressed in the forward model error covariance matrix, S_y (Equation 18). The largest source of uncertainty in the forward model is the clear sky radiative transfer. The uncertainty in the clear sky radiative transfer should include the effects of errors in the surface temperature, surface emissivity, and atmospheric profiles. Spatial heterogeneity is another source of error since the retrieval assumes that each pixel is uniformly cloudy. Instrumental issues, such as those due to calibration and noise effects, also contribute to the forward model error. Thus, the total uncertainty in the forward model is assumed to be composed of a linear combination of three major sources (see Equation 19): instrumental, clear sky radiative transfer modeling, and pixel heterogeneity. In Equation 19, the instrument uncertainty is given by σ^2_{instr}, the clear sky radiative transfer uncertainty is denoted by σ^2_{clr}, and the uncertainty due to pixel heterogeneity is given by σ^2_{hetero}. The impact of the clear sky radiative transfer uncertainty is approximately inversely proportional to the cloud emissivity, so it is weighted by the 11-μm cloud emissivity, ε(11μm). The off-diagonal elements (correlated uncertainty) of the forward model error covariance matrix are very difficult to determine, so only the diagonal elements (uncorrelated uncertainty) are considered.

$$S_y = \begin{pmatrix} \sigma^2_{BT(11\mu m)} & 0.0 & 0.0 \\ 0.0 & \sigma^2_{BTD(11-12\mu m)} & 0.0 \\ 0.0 & 0.0 & \sigma^2_{BTD(11-13.3\mu m)} \end{pmatrix} \quad \text{(Eq. 18)}$$

$$\sigma^2 = \sigma^2_{instr} + [1 - \varepsilon(11\mu m)]\sigma^2_{clr} + \sigma^2_{hetero} \quad \text{(Eq. 19)}$$

The uncertainty in the clear sky radiative transfer (σ^2_{clr}) is determined through a radiance bias analysis. The radiance bias estimates should be monitored over time and changes to σ^2_{clr} should be made accordingly. The current estimates of σ^2_{clr}, which are shown in ?????, are based on analysis of Spinning Enhanced Visible and Infrared Imager (SEVIRI) data. As expected, the uncertainty over land surfaces is larger than over open water. Over land, larger errors in surface temperature and surface emissivity results in larger radiance biases compared to water surfaces. It should be noted that the clear sky radiance biases will become smaller as clear sky radiative transfer models, numerical weather prediction models, and surface emissivity estimates improve.

The forward model uncertainty due to spatial heterogeneity (σ^2_{hetero}) is approximated by the variance of each observation used in the retrieval over a 3 x 3 pixel box centered on the current pixel of interest. The last and probably least significant forward model error term is that due to instrumental effects, σ^2_{instr}. This term includes noise, calibration, and spectral response errors. The current conservative estimates of this uncertainty are given in Table 2- 3. Similar to the uncertainty estimates associated with the clear sky radiative transfer, these will need to be updated during the early orbit period.

Table 2- 3 The individual components of the total forward model uncertainty used in the 3-channel volcanic ash retrieval. The total uncertainty is given by Equation 19. These values need to be squared when building the matrix given by Equation 18.

Parameter	Instrument Uncertainty (σ_{instr})	Clear Sky Radiance Uncertainty (σ_{clr}) (Land, Water)	Non-uniform Pixel Uncertainty (σ_{hetero})
$\sigma_{BT(11\mu m)}$	0.25 K	5.0 K, 0.5 K	variable (see text)
$\sigma_{BTD(11-12\mu m)}$	0.25 K	1.0 K, 0.5 K	variable (see text)
$\sigma_{BTD(11-13.3\mu m)}$	0.5 K	4.0 K, 1.0 K	variable (see text)

For the two-channel retrieval, the physical reasoning described in the preceding subsection applies to the forward model, except fewer channels are used. For sensors with the lack of 13.3 μm channel, Equations 15 and 17 are not applicable and Equation 18 is reduced by eliminating the bottom row and right most column to become a 2x2 matrix. The individual components of the total 2-channel forward model uncertainty are given in Table 2- 4.

Table 2- 4 The individual components of the total forward model uncertainty used in the VIIRS volcanic ash retrieval. The total uncertainty is given by Equation 19. These values need to be squared when building the matrix given by Equation 18.

Parameter	Instrument Uncertainty (σ_{instr})	Clear Sky Radiance Uncertainty (σ_{clr}) (Land, Water)	Non-uniform Pixel Uncertainty (σ_{hetero})
$\sigma_{BT(11\mu m)}$	0.50 K	5.0 K, 0.5 K	variable (see text)
$\sigma_{BTD(11\text{-}12\mu m)}$	0.25 K	1.0 K, 0.25 K	variable (see text)

2.3.2.6 Optimal Estimation Iterations

Each step in the optimal estimation iteration changes each element of x as governed by the following relationship

$$\delta x = S_x\{K^T S_y^{-1}[y - f(x)] + S_a^{-1}(x_a - x)\} \quad \text{(Eq. 20)}$$

where δx is the amount by which x is incremented during a given retrieval iteration and S_x is error covariance matrix of x and K is the Kernel or Jacobian matrix. The Kernel matrix contains the partial derivatives of each element of f to each element of x as follows (*for 2-channel implementation, Kernel references to the 13.3 μm should be ignored)*.

$$K = \begin{pmatrix} \frac{\partial BT(11\mu m)}{\partial T_{eff}} & \frac{\partial BT(11\mu m)}{\partial \varepsilon(11\mu m)} & \frac{\partial BT(11\mu m)}{\partial \beta(12/11\mu m)} \\ \frac{\partial BTD(11-12\mu m)}{\partial T_{eff}} & \frac{\partial BTD(11-12\mu m)}{\partial \varepsilon(11\mu m)} & \frac{\partial BTD(11-12\mu m)}{\partial \beta(12/11\mu m)} \\ \frac{\partial BTD(11-13.3\mu m)}{\partial T_{eff}} & \frac{\partial BTD(11-13.3\mu m)}{\partial \varepsilon(11\mu m)} & \frac{\partial BTD(11-13.3\mu m)}{\partial \beta(12/11\mu m)} \end{pmatrix} \quad \text{(Eq. 21)}$$

Given our choice of forward model, an analytical expression for each element of K can be derived from Equations 13 – 17, Equation 6, and the Planck Function. The derivative of each of the forward model simulated observations with respect to T_{eff} is given by the following set of equations. In these equations, $\partial B(\lambda)/\partial T_{eff}$ is the derivative of the Planck Function with respect to the effective cloud temperature, T_{eff}, and $\partial B(\lambda)/\partial T$ is the derivative of the Planck Function with respect to the forward model derived brightness temperature. All other symbols have been previously defined.

$$\frac{\partial BT(11\mu m)}{\partial T_{eff}} = \varepsilon(11\mu m)t_{ac}(11\mu m)\left(\frac{\partial B(11\mu m)}{\partial T_{eff}}\right)\left(\frac{\partial B(11\mu m)}{\partial T}\right)^{-1}$$ (Eq. 22)

$$\frac{\partial BTD(11-12\mu m)}{\partial T_{eff}} = \frac{\partial BT(11\mu m)}{\partial T_{eff}} - \varepsilon(12\mu m)t_{ac}(12\mu m)\left(\frac{\partial B(12\mu m)}{\partial T_{eff}}\right)\left(\frac{\partial B(12\mu m)}{\partial T}\right)^{-1}$$ (Eq. 23)

$$\frac{\partial BTD(11-13.3\mu m)}{\partial T_{eff}} = \frac{\partial BT(11\mu m)}{\partial T_{eff}} - \varepsilon(13.3\mu m)t_{ac}(13.3\mu m)\left(\frac{\partial B(13.3\mu m)}{\partial T_{eff}}\right)\left(\frac{\partial B(13.3\mu m)}{\partial T}\right)^{-1}$$ (Eq. 24)

The following equations give the derivative of each forward model simulation with respect to $\varepsilon(11\mu m)$.

$$\frac{\partial BT(11\mu m)}{\partial \varepsilon(11\mu m)} = [R_{cld}(11\mu m) - R_{clr}(11\mu m)]\left(\frac{\partial B(11\mu m)}{\partial T}\right)^{-1}$$ (Eq. 25)

$$\frac{\partial BTD(11-12\mu m)}{\partial \varepsilon(11\mu m)} =$$

$$\frac{\partial BT(11\mu m)}{\partial \varepsilon(11\mu m)} - [R_{cld}(12\mu m) - R_{clr}(12\mu m)][\beta(12/11\mu m)(1-\varepsilon(11\mu m))^{\beta(12/11\mu m)-1}]\left(\frac{\partial B(12\mu m)}{\partial T}\right)^{-1}$$
(Eq. 26)

$$\frac{\partial BTD(11-13.3\mu m)}{\partial \varepsilon(11\mu m)} =$$

$$\frac{\partial BT(11\mu m)}{\partial \varepsilon(11\mu m)} - [R_{cld}(13.3\mu m) - R_{clr}(13.3\mu m)][\beta(13.3/11\mu m)(1-\varepsilon(11\mu m))^{\beta(13.3/11\mu m)-1}]\left(\frac{\partial B(13.3\mu m)}{\partial T}\right)^{-1}$$
(Eq. 27)

Finally, the derivative of each forward model simulation with respect to $\beta(12/11\mu m)$ is given by the following equations. In Equation 30, $\partial\beta(13.3/11\mu m)/\partial\beta(12/11\mu m)$ is applied to Equation 6 *(3-channel retrieval only)*.

$$\frac{\partial BT(11\mu m)}{\partial \beta(12/11\mu m)} = 0.0$$ (Eq. 28)

$$\frac{\partial BTD(11-12\mu m)}{\partial \beta(12/11\mu m)} = [R_{cld}(12\mu m) - R_{clr}(12\mu m)]\ln[1-\varepsilon(11\mu m)][1-\varepsilon(12\mu m)]\left(\frac{\partial B(12\mu m)}{\partial T}\right)^{-1}$$
(Eq. 29)

$$\frac{\partial BTD(11-13.3\mu m)}{\partial \beta(12/11\mu m)} =$$
$$[R_{cld}(13.3\mu m) - R_{clr}(13.3\mu m)]\ln[1-\varepsilon(11\mu m)][1-\varepsilon(13.3\mu m)]\left(\frac{\partial \beta(13.3/11\mu m)}{\partial \beta(12/11\mu m)}\right)\left(\frac{\partial B(13.3\mu m)}{\partial T}\right)^{-1}$$ (Eq. 30)

Once the Kernel Matrix has been calculated, the error covariance matrix of x (Equation 31) can be determined using Equation 32 (Rodgers, 1976).

$$S_x = \begin{pmatrix} \sigma^2_{Teff} & 0.0 & 0.0 \\ 0.0 & \sigma^2_{\varepsilon(11\mu m)} & 0.0 \\ 0.0 & 0.0 & \sigma^2_{\beta(12/11\mu m)} \end{pmatrix}$$ (Eq. 31)

$$S_x = (S_a^{-1} + K^T S_y^{-1} K)^{-1}$$ (Eq. 32)

The optimal estimation approach is run until the following convergence criterion is met.

$$\left\| \sum \delta x S_x^{-1} \delta x \right\| \leq \frac{p}{2}$$ (Eq. 33)

Where p is the size of x, which is 3 in our case. This convergence criterion is taken out of Rodgers (1976). If the retrieval does not converge after 10 iterations, it is deemed a failed retrieval. In the event of a failed retrieval, all retrieved parameters are set to missing, not the *a priori* values. The *a priori* values are not used since ash cloud properties are highly variable in time and space and cannot be accurately parameterized by guess values alone. Very few retrievals (< 0.01%) fail to converge, so this has a negligible impact on the ash products. Further, δx is constrained such that the maximum allowed absolute changes in the retrieved parameters, T_{eff}, ε(11μm), and β(12/11μm), are 20.0 K, 0.3, 0.2, respectively. Once the retrieval vector is updated by δx, the retrieved parameters are constrained to be within a certain physically based range. Table 2- 5 shows the allowed min and max values of each retrieved parameter.

Table 2- 5 The valid range for each retrieved parameter.

Parameter	Minimum Allowed Value	Maximum Allowed Value
T_{eff}	160 K	330 K
$\varepsilon(11\mu m)$	0.0	1.0
$\beta(12/11\mu m)$	0.20	1.05

2.4 Algorithm Output

The VOLCAT output consists of three main types. The VOLCAT 'Event Files' contain information about the spatial and temporal location of volcanic ash, as well as retrieved physical properties of the volcanic ash clouds, including ash cloud top height, column ash mass loading, and ash particle effective radius. The VOLCAT event file output will be generated as part of the Stage 1 operational transition and is described below. The VOLCAT system also creates volcanic eruption alerts. These alerts can be delivered to end-users at their discretion and include formats of web-based alerts, email alerts, or text message alerts. The VOLCAT eruptive alerts will be part of the Stage 2 operational transition, which will follow successful Stage 1 implementation. These VOLCAT outputs will be briefly described in the current document but will be further described in future document updates. The VOLCAT system also outputs high-spectral resolution IR sounder-based daily global SO_2 composites for each supported low Earth orbit satellite. The SO_2 composites include spatial and temporal location of SO_2 as well as retrieved physical properties including SO_2 cloud top height and column SO_2 mass loading. Similar to eruptive alerts, global SO_2 composites will be part of the Stage 2 operational transition. Like the eruptive alerts, the VOLCAT SO_2 output will be briefly described in the current document but will be further described in future document updates. Further detail about each output type and which user requirements the products address follows.

The VOLCAT event files are produced when the VOLCAT system is actively detecting and tracking a volcanic cloud. The VOLCAT event files are created on a sensor and volcano basis and cover a small geographical domain (relative to the full satellite scan domain and yet fully encompasses the row/column pixel extent of the detected volcanic cloud(s)). For example, for a VOLCAT volcanic cloud detection using GOES-16 ABI Fulldisk observations from the Fuego volcano in Guatemala, a file would be generated that contains satellite sensor, scan domain and volcano ID (among other information). The VOLCAT event file contains many useful outputs, the most fundamental outputs include detection (e.g., pixel locations) of volcanic clouds and the corresponding physical properties (e.g., ash cloud-top height and ash column mass loading). The VOLCAT event files, and contents within, relay information pertinent to the various VOLCAT requirements. Later sections of this document demonstrate the various VOLCAT requirements and show how the VOLCAT system is meeting the requirements. Full requirements can be found in the VOLCAT CDR slides—ATB supplemental. In addition to VOLCAT event files, VOLCAT event JSON files are created. The VOLCAT event JSON files are small, easily downloaded files by end-users that can then be used to determine if a user needs to download the full event netcdf file.

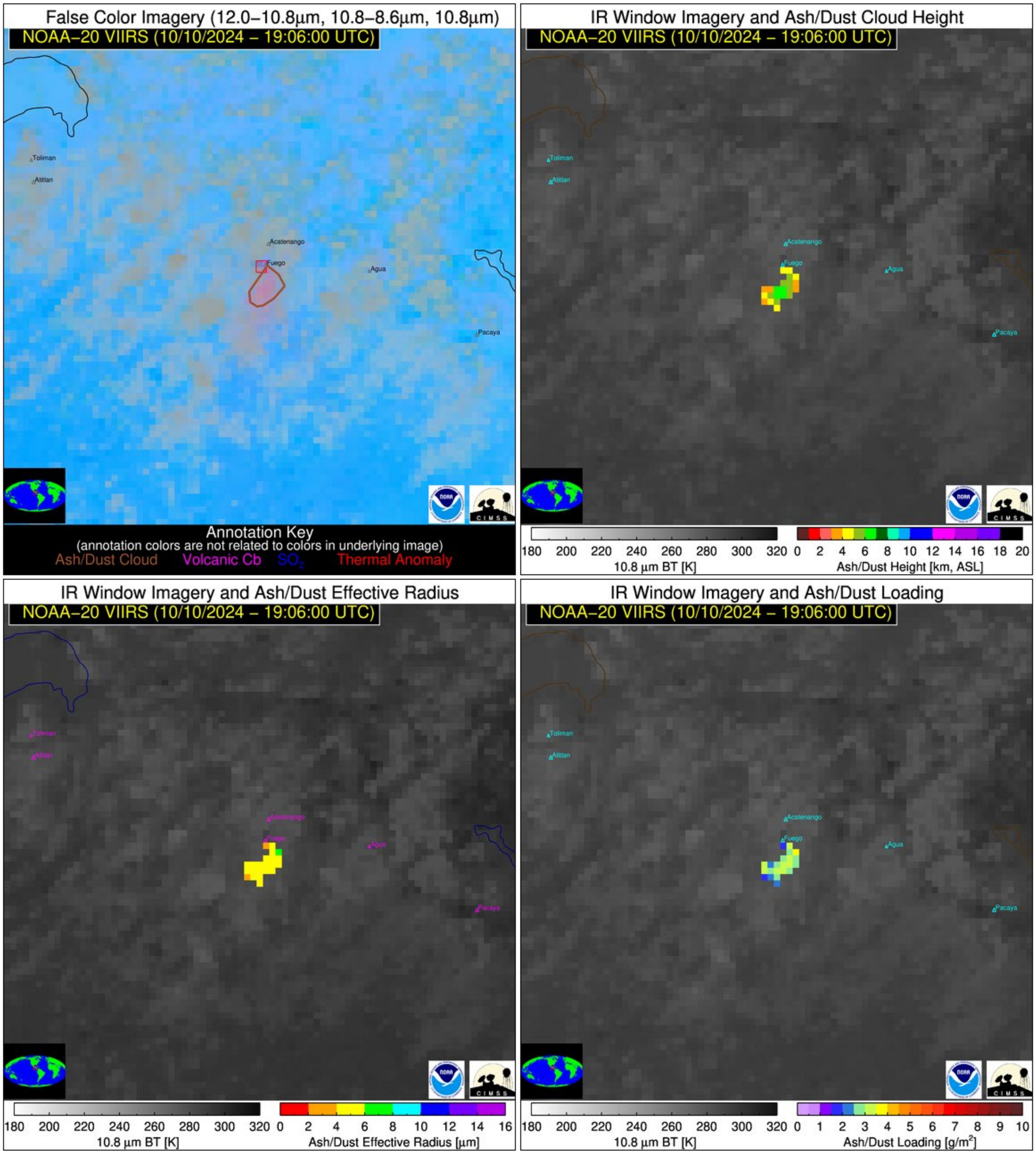

Figure 2- 10 A 4-panel image depiction of the most fundamental VOLCAT event file output fields. The upper left panel is a false color RGB image comprised of infrared window brightness temperatures and brightness temperature differences. The VOLCAT ash cloud detection is depicted by the brown polygon in the RGB image. The remaining panels show infrared brightness temperature (grayscale)

and VOLCAT ash cloud property retrievals (ash cloud top height, upper right; ash cloud particle effective radius, lower left; and ash column mass loading, lower right).

Figure 2- 10 is an image depiction of the most fundamental VOLCAT event file output fields. The VOLCAT event files contain many outputs, but most fundamental to end-user requirements are automated detection and tracking of volcanic clouds and their physical properties. In the example above a small volcanic cloud was produced by the Fuego volcano in Guatemala on October 10, 2024, and was observed by NOAA-20 VIIRS. The VOLCAT event files contain 2-d pixel variables containing yes/no ash detection flag and 2-d pixel variables for physical properties, like ash cloud-top height and ash column mass loading. The VOLCAT event files also contain other useful fields, including 2-d selected pixel brightness temperatures, polarimetric fields centered on source volcano, scalar variables like total mass loaded integrated over all ash containing pixels, etc.

While automated delivery of eruptive alerts are part of the Stage 2 VOLCAT transition to operations, the data processing aspect of the Stage 1 transition is a fundamental step in creating automated eruptive alerts. Figure 2- 11 shows examples of VOLCAT automated eruptive alert text messages and emails. The automated eruptive alerts are designed to achieve the smallest latency for notification of new eruptive events as possible. A subscription is required to receive the automated eruptive alerts notifications that is customizable via the VOLCAT website (currently experimental and hosted at University of Wisconsin – Space Science and Engineering Center). The automated eruptive alerts contain limited critical information and include a link for additional information and associated imagery hosted on the VOLCAT website (Figure 2- 12). Further details related to automated eruptive alerts will be included in an updated document when complete details related to Stage 2 VOLCAT transition is known.

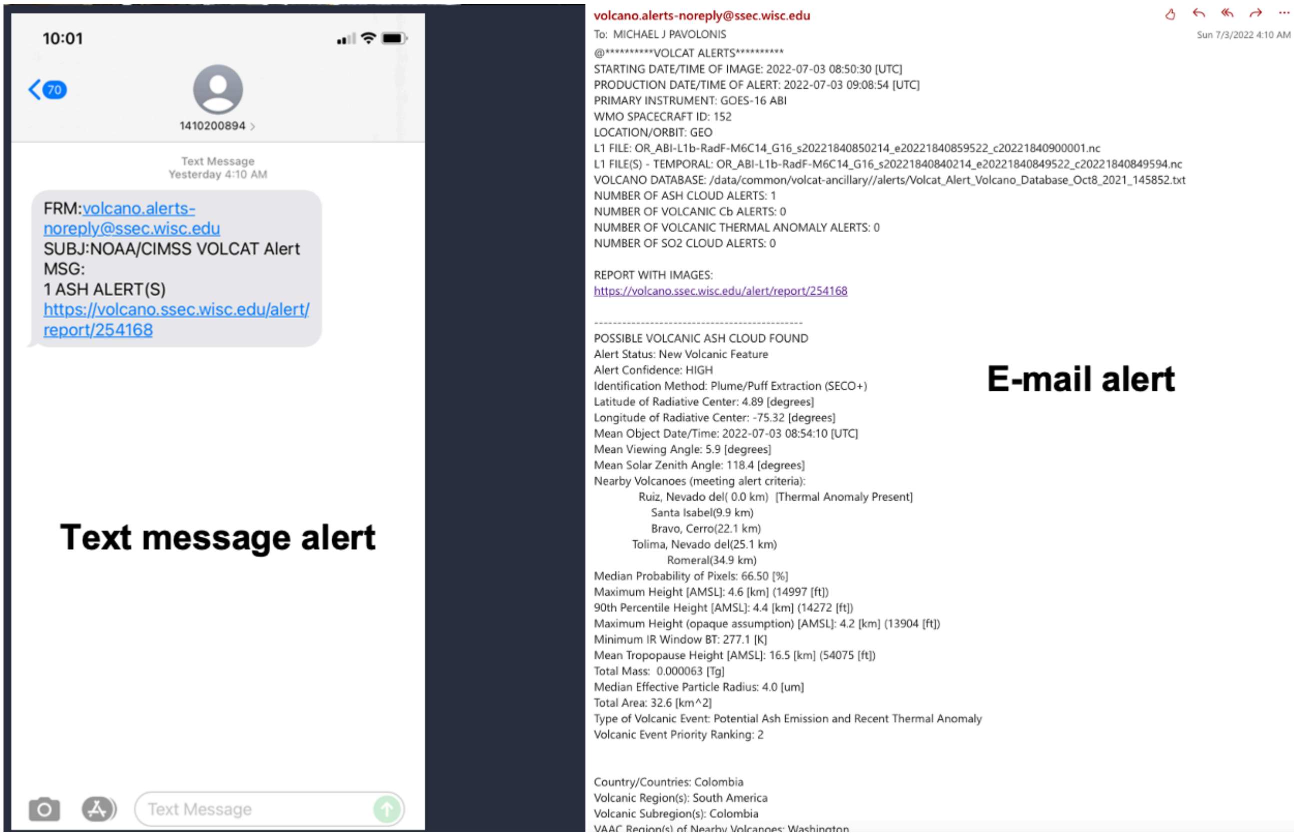

Figure 2- 11 Automated VOLCAT eruptive alerts that end-users can optionally subscribe to using the experimental VOLCAT website hosted at University of Wisconsin – Space Science and Engineering Center. Users can select text message and/or email alert delivery options, along with a variety of customization based on Volcanic Ash Advisory Center region, geographical region, etc.

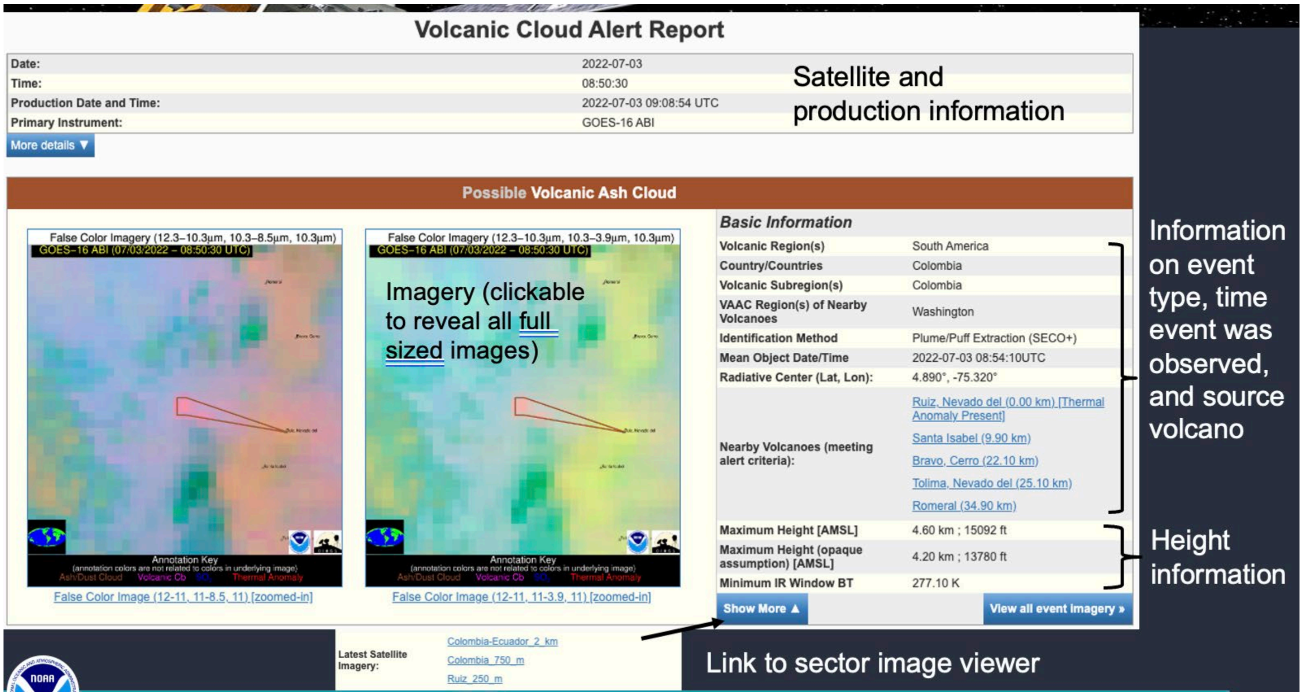

Figure 2- 12 An example of a VOLCAT alert link available from the automated eruptive alert messages. The VOLCAT alerts are hosted on the VOLCAT website and contain automated imagery zoomed on the volcanic feature. The text provides a variety of other useful information, including source volcano, maximum volcanic cloud height, links to additional imagery, etc.

The VOLCAT SO_2 user requirements are addressed by algorithms that utilize broadband imagers and high spectral resolution infrared sounders, like VIIRS and CrIS. The usage of high spectral resolution infrared sounders to detect and characterize SO_2 is necessary given the spectrally narrow absorption lines related to SO_2. The VOLCAT SO_2 algorithms provide information on SO_2 cloud top height and SO_2 column mass loading. An example of a NOAA-20 VIIRS+CrIS derived daily global SO_2 column mass loading map is shown in Figure 2- 13. The VOLCAT SO_2 product suite will be part of the Stage 2 VOLCAT transition to operations and more details will be provided in an updated document at that time.

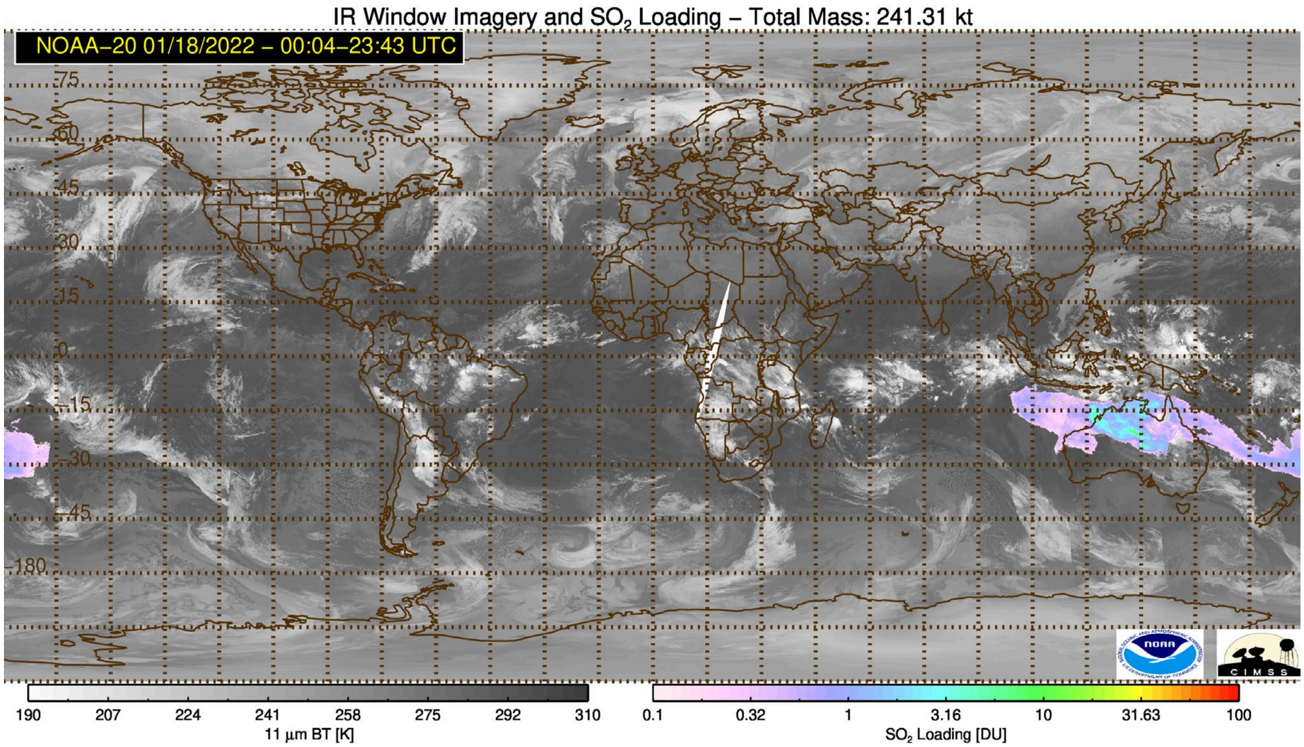

Figure 2- 13 An image of a daily VOLCAT SO_2 mass loading composite derived from NOAA-20 VIIRS+CrIS observations. The large SO_2 cloud over the southern hemisphere is from the Honga Tunga volcano that erupted in January 2022.

2.5 Performance Estimates

2.5.1 Test Data Description

The VOLCAT science team utilizes several different approaches for validation and verification of the VOLCAT output. Each of these approaches are briefly described in this section, along with the user requirements addressed by the validation and verification. Table 2- 6 summarizes the validation and verification techniques, with further details in Section 2.5.3.

VOLCAT validation and verification uses data from each scanning domain for each supported satellite instrument. For example, for GOES-ABI this includes Fulldisk, CONUS, Mesoscale1 and Mesoscale2 scanning domains or for sensors like VIIRS only one scanning domain exists. Since volcanic ash clouds are spatially and temporally rare, random usage of satellite data for validation is not a suitable approach. For validation and verification, expert knowledge is required to find volcanic eruptions and analyze satellite imagery to determine what period(s), if any, are suitable for inclusion in a validation and verification dataset. This expert analysis is performed by the VOLCAT science team. The VOLCAT science team uses information from Volcanic Ash Advisory Centers, volcano observatories, the Smithsonian Global Volcanism Project, satellite data processing, news stories, etc. to find potential cases and then must analyze each case to see if it is suitable for inclusion (e.g., recall requirements define volcanic ash must be top cloud layer to be suitable, etc.). This case selection effort is intensively performed when a new satellite sensor becomes available to ensure the VOLCAT results using the new satellite sensors are meeting requirements. After a satellite sensor is fully validated, this process is repeated on a more infrequent, case study basis, as needed.

Table 2- 6 VOLCAT validation techniques and VOLCAT requirements addressed by each validation technique.

Validation Technique	Validation Technique Purpose
Cloud Advection Pattern Assessment	Primary validation technique for ash cloud-top height and ash mass loading validation (address height and mass loading accuracy requirements).
Cloud Detection and Tracking Validation	Primary validation technique for detection contingency table statistics and cloud tracking statistics (address detection and tracking requirements).
Emergent Cloud Alerting Validation	Primary validation technique for alerting requirements.
Supplemental Volcanic Cloud Property Validation	Secondary approach for ash cloud-top height and ash mass loading validation (data matchups are rare; so only used as supplemental analysis).

Beyond VOLCAT validation and verification, test cases for each supported sensor are maintained to ensure externally shared VOLCAT processing system software containers are producing expected results from a computer science/implementation perspective.

2.5.2 Sensor Effects

Poor data quality in the instrument observations can adversely affect VOLCAT products. For example, sensor noise, missing scan chunks, and irregular spectral effects can all be problematic. This section briefly addresses known issues and possible mitigation strategies.

2.5.2.1 Band-to-Band Co-Registration Errors

The VOLCAT applications are sensitive to band-to-band co-registration errors. Co-registration errors can lead to increased errors in VOLCAT detections and retrievals. Sensors for observations for each satellite channel can be located on different electronic boards on the satellite instruments. For example, the 8.5 μm channel is often located on a different board than the long-wave IR-window and CO_2 channels (10, 11, 12, and 13.3 μm channels). Co-registration errors between the 8.5 μm channel and the long-wave IR window channels can lead to increased false VOLCAT detections. The co-registration between these channels is easily identified by having sufficiently zoomed volcanic ash false color RGB imagery, especially in scenes containing deep convective clouds. Co-registration errors appear most frequently during the checkout period of a new satellite sensors and are often quickly corrected. Uncorrectable co-registration errors could require mitigation research by the VOLCAT science team should this scenario be encountered but at present such errors do not exist with the current satellite constellation.

2.5.2.2 Calibration

The data for each input satellite channel must be well-calibrated for optimal VOLCAT performance. The VOLCAT system contains internal radiative transfer calculations for computing clear sky radiances. To determine calibration errors, clear-sky radiance biases can be computed for each satellite channel. Clear-sky radiance biases are computed by manually identifying clear pixels in satellite imagery (e.g., no clouds) and computing the differences between observed radiances and computed clear-sky radiances (or brightness temperatures). The best locations for this analysis are over ocean as surface emissivity errors are smaller than over land surfaces. The expected biases should be centered around 0.0 with small standard deviations; unexpectedly large biases (e.g., not centered around 0.0 or large standard deviations) suggest calibration errors and require further manual investigation. These errors occur most frequently during the checkout period of a new satellite sensor and are often quickly corrected. The current operational satellite constellation does not contain any satellites with problematic calibration errors.

2.5.2.3 Sensor Noise/Irregular Spectral Effects

Sensor noise and/or irregular spectral effects can adversely impact VOLCAT results. The VOLCAT system has multiple checks to attempt to mitigate impacts from any of these type effects. The primary checks act to screen bad pixels on a by-channel basis where L1b QFs indicate poor data quality. Depending on the number of bands with poor quality pixels, the impacts can range from none to significant if large chunks of necessary bands do not have usable data. Additionally, the VOLCAT system computes internal scan-line related metrics to further check for poor input data on a per satellite input channel basis that does not meet the level of bad L1b QFs. When these scenarios are encountered, scan lines where problematic data is indicated will be excluded. Lastly, GOES-17 ABI was known to have poor L1b data quality in some channels in some portions of the year related to a problem with the loop heat pipe cooling system. To mitigate effects with the VOLCAT system, an analysis was performed to determine at which focal plane temperature each ABI channel would become detrimental to VOLCAT products and exclude the degraded channel(s) when the focal plane temperature threshold was exceeded. In these scenarios VOLCAT operated with a more limited channel set, but products still were derived if a minimum number of channels were available. Sensor noise/irregular spectral effects can have a large range of impacts to the VOLCAT application depending on the severity, number of pixels, or number of channels impacted by poor quality input data.

2.5.2.4 Missing chunks/channels

A common source of error occurs when the satellite sensor (or ground system) produces missing scanline chunks. This can be due to several reasons, including eclipse season. In these scenarios, one or more of the channels are missing in the scene. The missing chunks can impact a portion of a scanning domain or an entire channel can be missing for an observation set. Depending on the number of channels and which channels are impacted, the impacts can range significantly—from no impact to making the VOLCAT application exit and unable to generate products for a given observation set.

2.5.3 Retrieval Errors

This section highlights quantitative validation and verification of the datasets described in Section 2.5.1. Possible sources of error are also listed.

A common theme to all VOLCAT requirements and subsequent validation analysis is the volcanic ash must be the top cloud layer, otherwise cases are not included in the validation assessments. In-situ observations of volcanic ash are not available (it is not practical nor safe (in general) to fly aircraft into volcanic ash clouds to make in-situ observations). As such it is necessary to validate volcanic ash products vicariously using a variety of techniques. The VOLCAT validation techniques are described in each subsection below.

2.5.3.1 Validation and Verification

2.5.3.1.1 Cloud Advection Pattern Assessment

The primary source of VOLCAT ash property validation is conducted using a cloud advection pattern assessment. The cloud advection pattern assessment requires meteorological and satellite observation expertise to 1) identify volcanic eruptions in satellite observations near volcanic vents, 2) derive volcanic cloud motion estimates (speed and direction) utilizing geostationary imagery, 3) using meteorological radiosonde observations, determine the altitude at which the derived volcanic cloud motion and observed wind speed and direction align (if possible and if sufficient vertical wind shear exists), and 4) using satellite observations, manually outline a polygon for the extent of volcanic ash in satellite imagery. For cases that meet the meteorological constraints, the error of the VOLCAT ash height retrieval is computed. Since mass loading cannot be inferred directly like the ash height, the VOLCAT mass loading error estimates are derived using the cloud advection pattern height as truth. Using the cloud advection pattern height as input, the corresponding mass loading value from the VOLCAT physical retrieval process is used to compute VOLCAT derived mass loading retrieval. An example of this analysis follows.

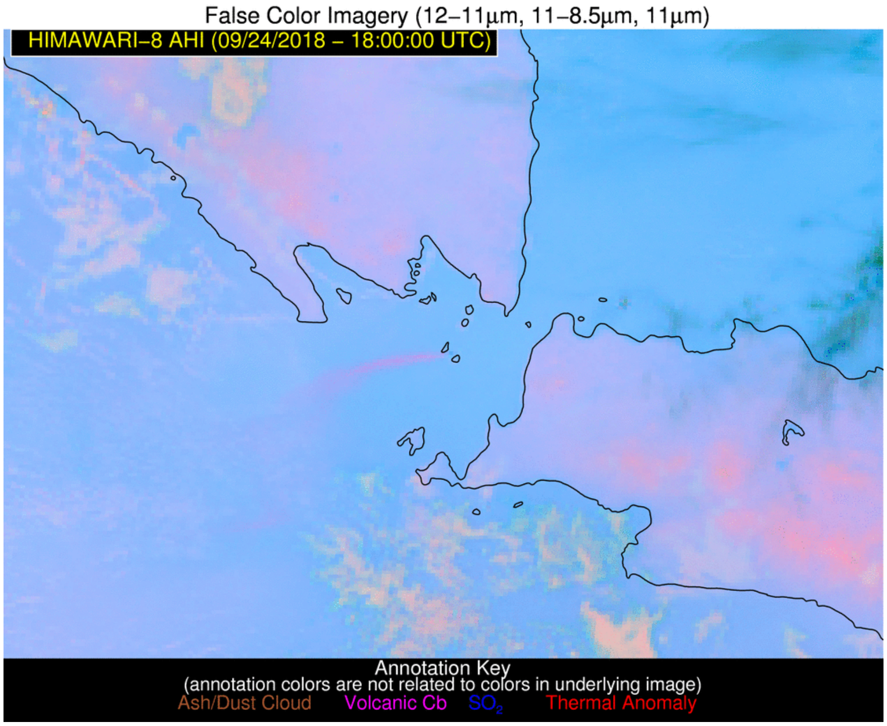

Figure 2- 14 The above loop shows a volcanic plume originating from the Krakatoa volcano in Indonesia as observed by Himawari-8 on September 24, 2018. The volcanic plume advection (speed and direction of movement) is used to estimate the wind speed and direction moving the cloud away from the volcanic vent.

Figure 2- 14 shows a newly emerging volcanic cloud in Himawari-8 imagery, in this case from the Krakatoa volcano in Indonesia during September 2018. The science team utilizes these satellite observations to complete steps 1 and 2 previously described. The analysis based on this geostationary imagery determined the volcanic cloud motion to be approximately 10 knots from 65 degrees. Next the analysis requires use of nearby radiosonde observations, in this case from the Jakarta observing station at 00 UTC September 25, 2018 (Figure 2- 15).

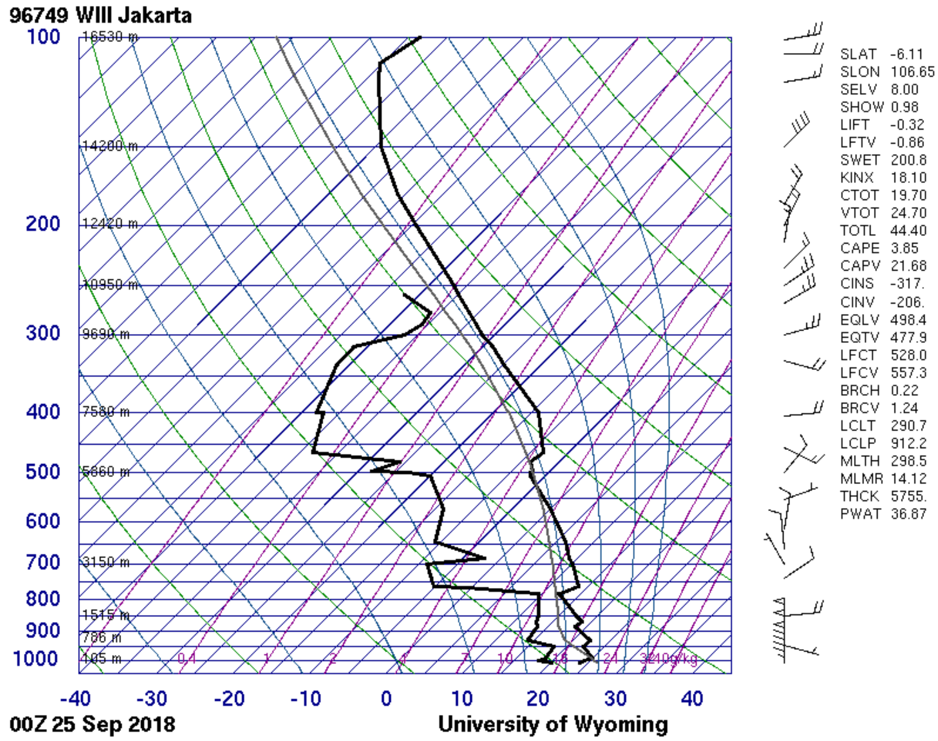

Figure 2- 15 A meteorological upper air radiosonde observation from Jakarta Airport in Indonesia on 00 UTC 25 September 2018 (credit University of Wyoming). The cloud advection derived motion of 10 knots at 65 degrees aligns with the radiosonde wind observations centered around 2500 meters ASL.

In this case the estimated volcanic cloud motion coincides with the upper air wind observations at approximately 2500 meters above sea level and this value is used as the cloud advection pattern derived truth height. It must be noted that sufficient vertical wind shear (wind must change speed and/or direction with increasing height) must be present for a case to be usable within the cloud advection pattern height analysis. Any case where the vertical wind shear does not allow for a truth height layer of 1 km or less must be discarded from the analysis (e.g., if the same wind speed/direction is present over a 3 km depth of the atmosphere the resultant range of truth far exceeds the accuracy requirements and must be discarded).

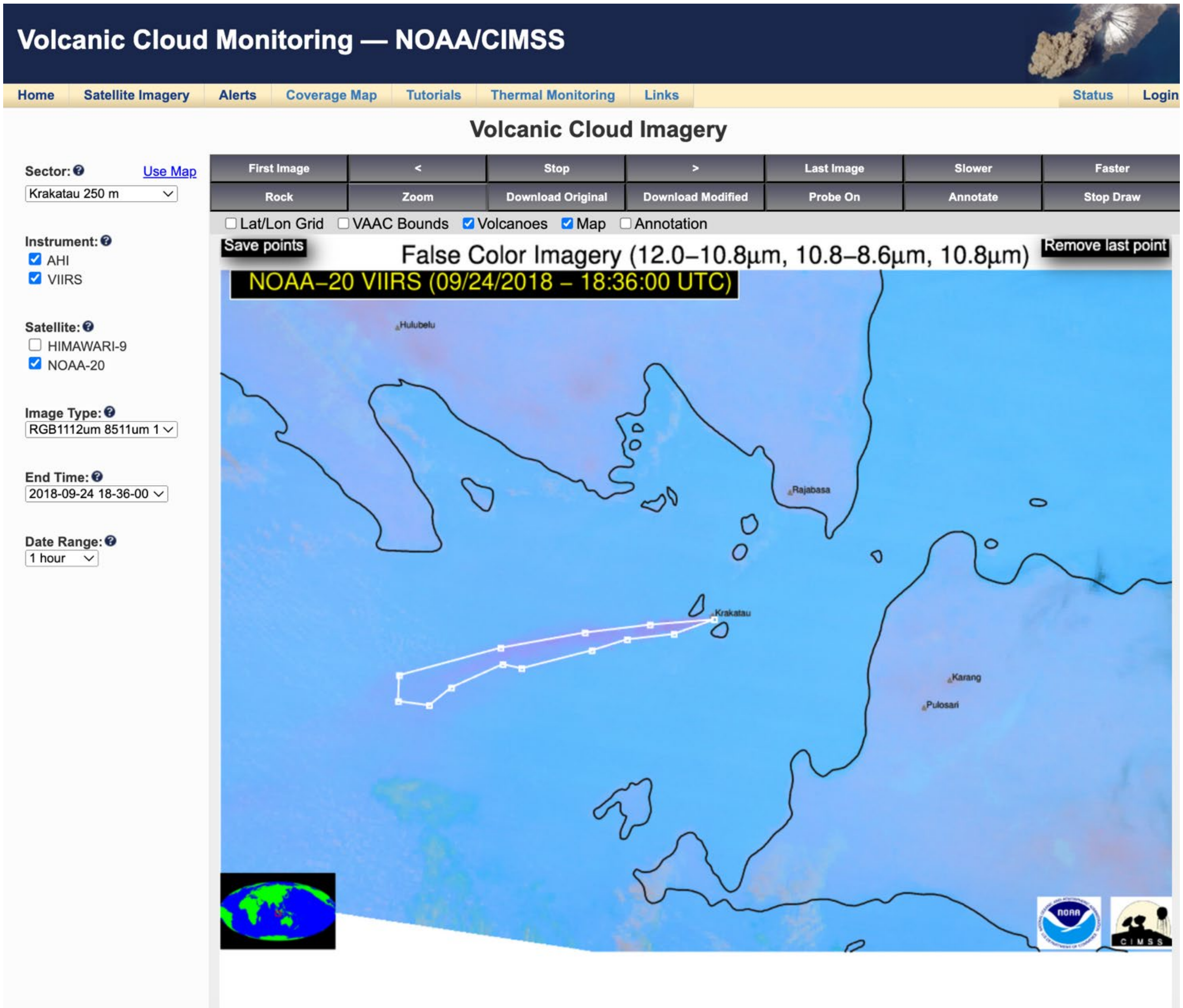

Figure 2- 16 An example of the web tool the VOLCAT science team uses to manually drawn polygons corresponding to the extent of volcanic ash in false color RGB satellite imagery. The polygon vertices latitude and longitude values are exported to a database and used in validation and verification statistical analysis.

The extent of volcanic ash in volcanic ash false color imagery is manually identified by science team experts. Figure 2- 16 is an example of the tool used to draw a polygon that represents extent of volcanic ash in imagery. The latitude and longitude of the drawn polygon vertices are exported and used in the last step of this process.

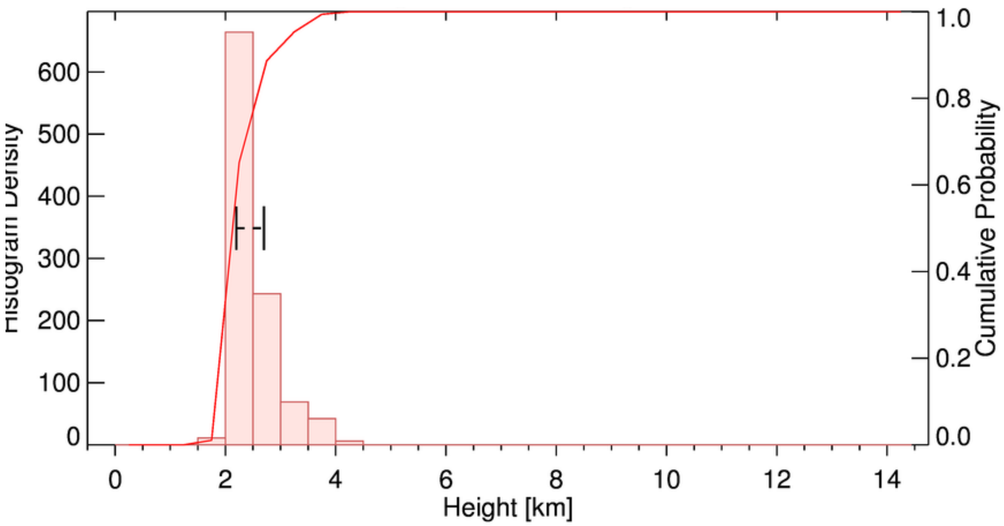

Figure 2- 17 An example of the cloud advection pattern truth height relative to VOLCAT ash cloud top height retrievals for the example shown in the previous figures (volcanic ash plume from Krakatoa volcano). The red histogram reflects VIIRS-derived VOLCAT ash cloud top height pixel counts and the black band represents the radiosonde-derived cloud height truth layer (the midpoint is used to formulate validation statistics).

Finally, the cloud advection pattern truth height (in this example 2500 meters) is used to compute error for each valid VOLCAT pixel contained in the manually drawn ash extent polygon in Figure 2- 16. Figure 2- 17 shows a schematic of this process, where the histogram red bars represent the VOLCAT ash height retrievals contained within the manually drawn polygon, and the black band represent the cloud advection pattern truth layer (midpoint is used to compute error). This process is repeated for many cases for each new satellite sensor to achieve a significant number of validated cases and pixels. Figure 2- 18 shows bulk results for VOLCAT ash height property retrieval and Figure 2- 19 shows bulk results for VOLCAT mass loading property retrieval derived from applying the approach for many cases.

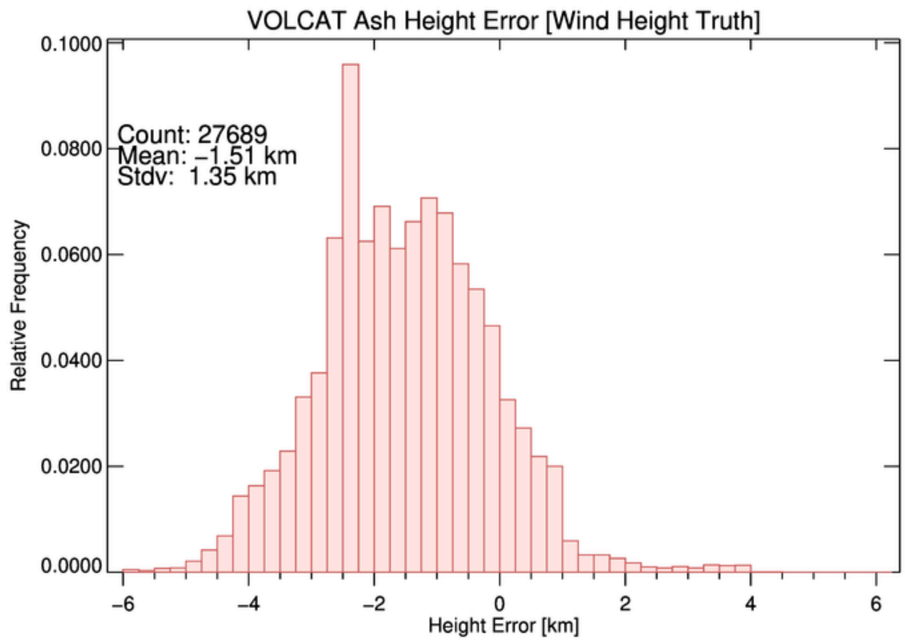

Figure 2- 18 VOLCAT ash cloud top height errors relative to cloud advection pattern truth values from many cases from a variety of satellite sensors. The ash cloud top height errors are well within the VOLCAT requirements.

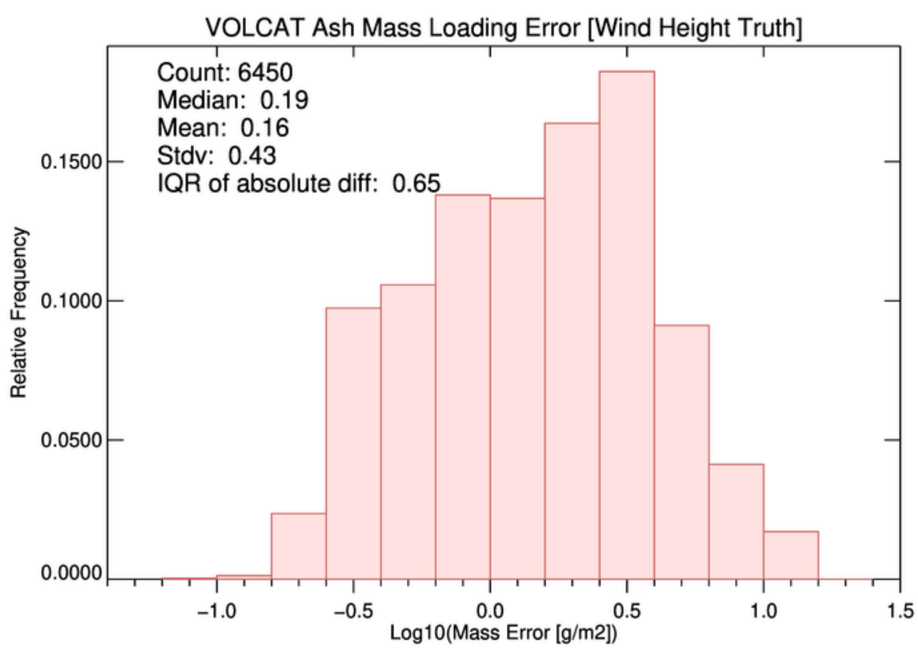

Figure 2- 19 VOLCAT ash mass loading errors (log10 based) relative to cloud advection pattern truth values from many cases from a variety of satellite sensors. The ash mass loading errors are well within the VOLCAT requirements.

The bulk analysis shows the VOLCAT ash height and mass loading retrievals are meeting the accuracy requirements.

2.5.3.1.2 Cloud Detection and Tracking Validation

The VOLCAT cloud detection and tracking requirements are validated through science team manual imagery analysis. The manual imagery analysis utilizes the tool shown in Figure 2- 16, where the science team draws a polygon to represent the outline of volcanic clouds in volcanic ash false color RGB imagery and the latitude and longitude of the polygon vertices are used to denote regions of volcanic clouds. The truth regions are combined with VOLCAT output to compute standard consistency table statistics which are used to compute commonly used statistics like probability of detection, false alarm ratio, critical success index (CSI), accuracy, etc. VOLCAT has different requirements for different states of volcanic eruptions/clouds. Figure 2- 20 shows the VOLCAT detection accuracy scores for the three different volcanic cloud stages, for all three types, the VOLCAT detection accuracy are well within product requirements. While CSI is not volcanic cloud detection/tracking requirement, it should be noted the CSI values are high for all three volcanic cloud types.

Umbrella cloud detection represents explosive volcanic eruptions that contain significant amount of water and ice particles, and these clouds do not typically exhibit the typical multispectral ash signature in the volcanic ash RGB imagery (typically pink to magenta tones). These clouds more resemble large meteorological cumulonimbus clouds and are defined as having mass loading values exceeding 10 g/m^2. The VOLCAT detection accuracy is found to be 99.6% for these cloud types, exceeding the 90% requirement.

Plume/puff detection represents volcanic clouds that typically exhibit classic multispectral ash signatures in volcanic ash RGB imagery (typically pink to magenta tones). These clouds range from near source volcanic vents to dispersed ash, which has been advected 10s to 100s of kilometers from the source vent and are defined as having mass loading values exceeding 1 g/m^2. The VOLCAT detection accuracy is found to be 99.7% for these cloud types, exceeding the 80% requirement.

Dispersed ash detection represents volcanic clouds that have been advected great distances from source volcanic vents, often 100s to 1000s of kilometers. These clouds exhibit classic multispectral signatures in volcanic RGB imagery, but often in a fainter manner as these clouds are well dispersed and can be approaching the limit of satellite detection. The dispersed ash clouds are defined as having mass loading exceeding 0.1 g/m^2. The VOLCAT accuracy was determined to be 99.5% for these clouds, exceeding the 70% requirement.

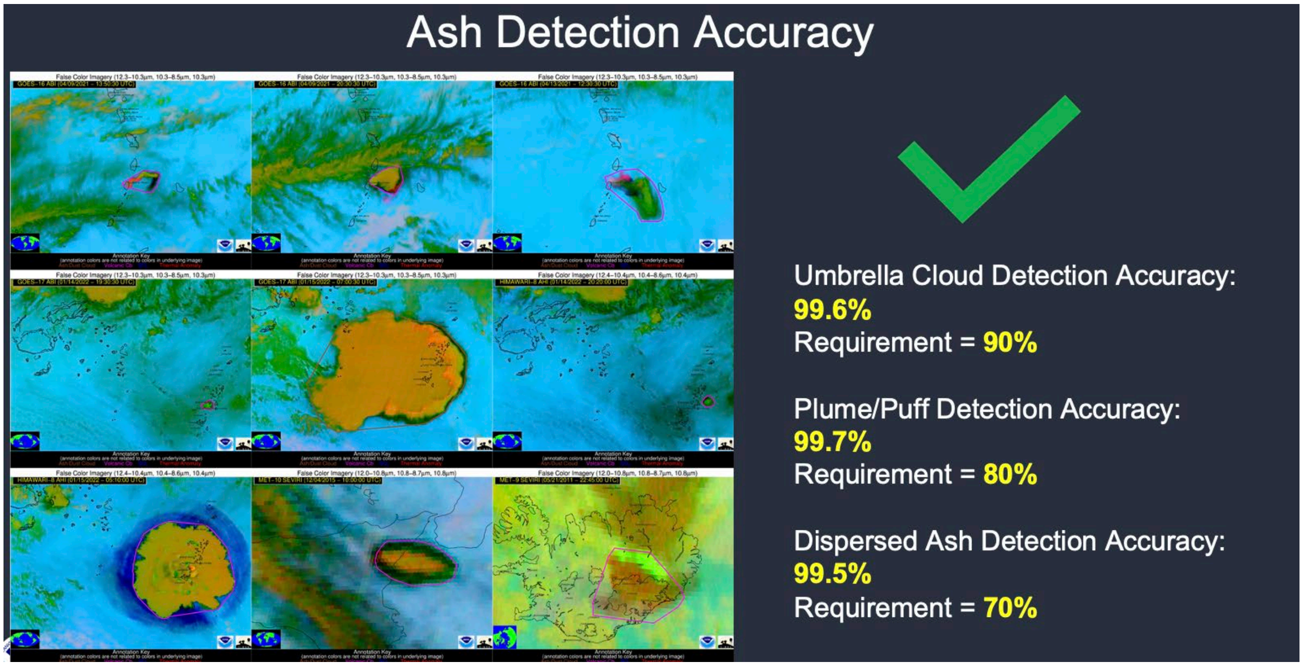

Figure 2- 20 VOLCAT bulk analysis of volcanic cloud detection and tracking accuracy results presented at the VOLCAT Critical Design Review.

2.5.3.1.3 Emergent Cloud/Alerting Validation

The automated detection of volcanic eruptions is necessary to attempt to meet ICAO stated requirements of 20-minute latency for notification of newly emergent volcanic eruptions. The volcanic eruption alerting requirements are written relative to human expert imagery analysis, which is the upper limit of performance. Figure 2- 21 shows a summary of VOLCAT eruptive alerting validation. All of these validation metrics rely on science team expertise in interpreting satellite imagery during and in wake of volcanic eruptions. The summary can be broken into four metrics, summary for each metric group follows.

Volcanic event detection is measured for volcanic emissions that create a detectable volcanic ash cloud that is discernable in imagery for 60 minutes or longer. The VOLCAT detection rate was 82% of these events, exceeding the requirement of 75%. The timeliness of initial detection of new volcanic emissions is measured using the first satellite observation in which the volcanic cloud is first unambiguously apparent. 79% of cases VOLCAT was able to meet these timeliness requirements, exceeding the 50% requirement. The VOLCAT system automatically attributes a detected volcanic cloud to a source volcano. In the source volcano analysis, the correct source volcano was attributed correctly in 100% of geostationary observations and 80% of low-Earth orbit observations, which exceed the requirement of 80%. The final emergent alerting requirement is related to false alarm rate. The requirement states that the false alarm rate must be 50% or less of produced volcanic alerts. The VOLCAT eruptive alert analysis indicated 54% of classifiable ash alerts were correct detections, exceeding the 50% requirement (here classifiable means expert analysis can indicate an alert is a correct detection or false alarm, ambiguous alerts are ignored in this analysis).

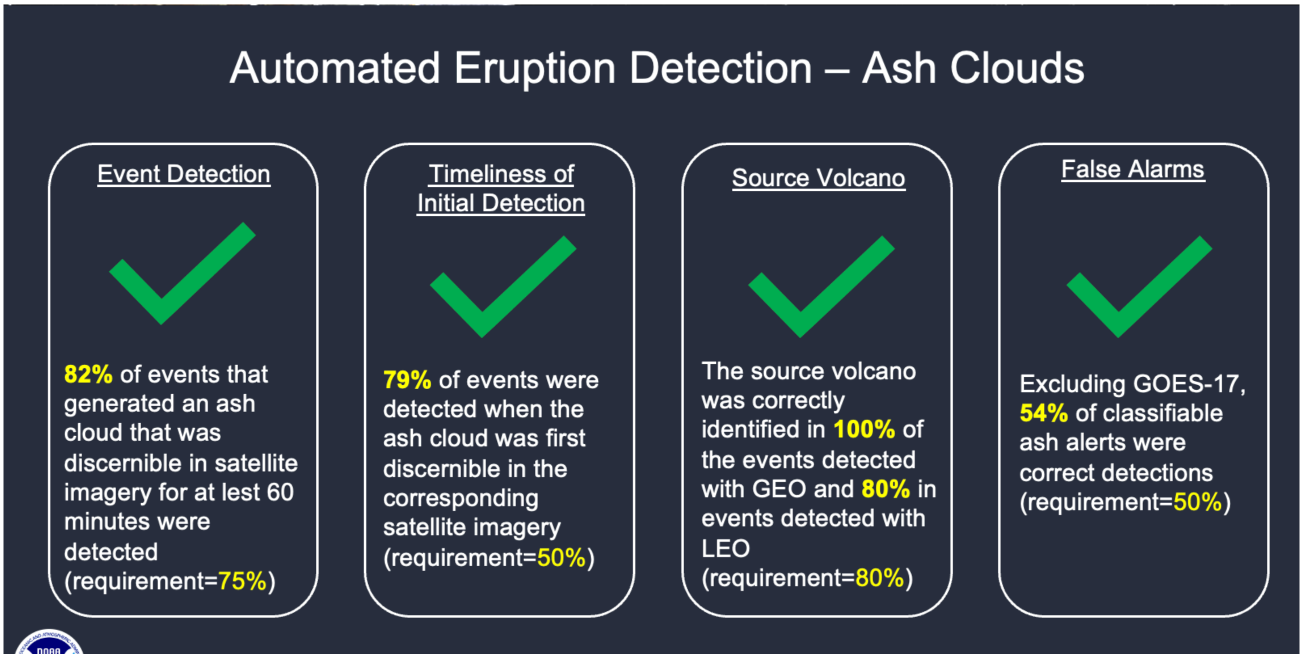

Figure 2- 21 VOLCAT bulk analysis of automated eruption detection accuracy results presented at the VOLCAT Critical Design Review.

2.5.3.1.4 Supplementary Volcanic Cloud Property Validation

The VOLCAT products are primarily validated through vicarious techniques and/or imagery analysis techniques, as direct remote sensing or in-situ observations of volcanic ash are exceedingly rare. However, direct remote sensing observations of volcanic ash or in-situ observations do occur on occasion, when these observations occur, the VOLCAT teams supplement the previous mentioned validation techniques with added analysis. This section demonstrates how direct remote sensing of volcanic clouds from space-borne lidar and how aircraft in-situ volcanic ash measurements were used to provide supplemental validation for some of the requirements. If these data are available in the future, the VOLCAT science team will utilize these datasets, if possible.

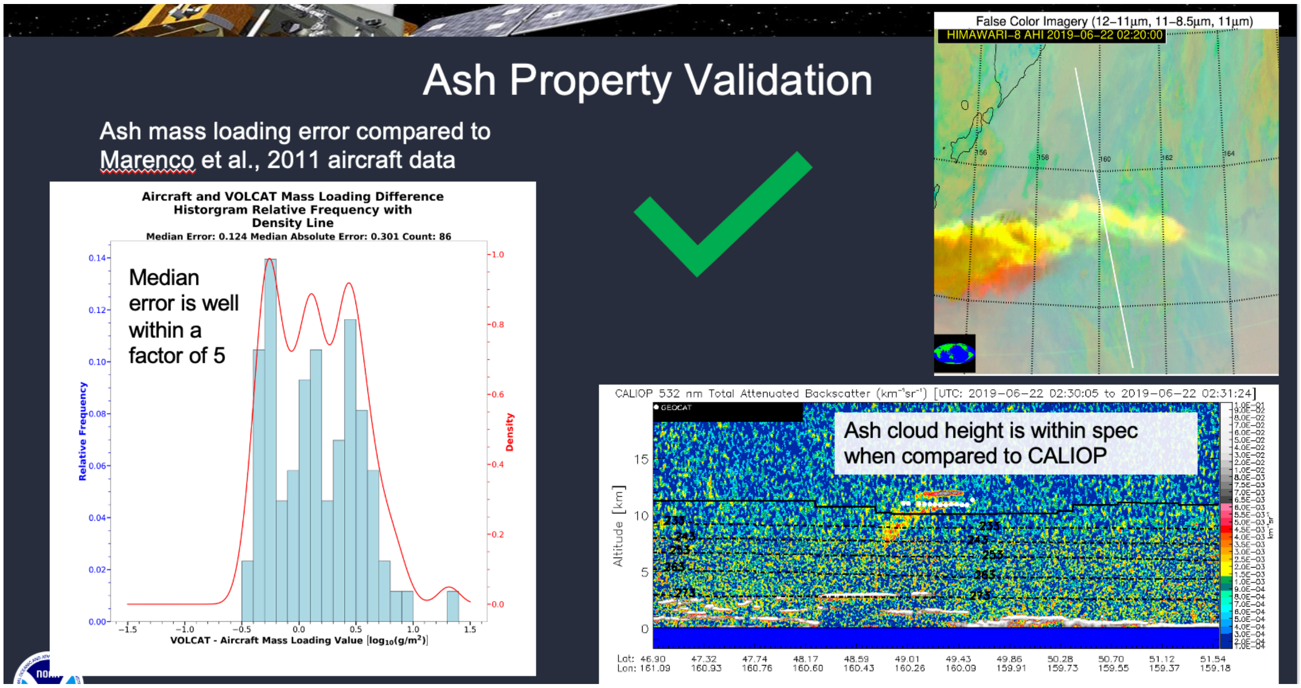

Figure 2- 22 Supplementary validation and verification techniques utilized by the VOLCAT science team. On the left are VOLCAT ash column mass loading error relative to in-situ aircraft volcanic ash mass loading observations. On the right are VOLCAT ash cloud height errors relative to space-borne lidar cloud boundary cloud height truth data.

Figure 2- 22 shows two examples of supplementary validation and verification analysis. The left is a comparison of VOLCAT mass loading retrievals, derived using Meteosat Second Generation SEVIRI data to aircraft in-situ mass loading data during the Eyjafjallajökull volcanic eruption in 2010. The data collection occurred over the Black Sea, when ash concentrations were low and damage to aircraft was reliably known to be minimal. The right is a comparison of VOLCAT ash cloud top height compared to space-borne lidar cloud height truth. Space-borne lidar cloud heights are accurate on the order of 10s of meters. Any available space-borne lidar observations of volcanic ash clouds co-located with passive satellite observations will be analyzed on an as-needed basis.

2.5.3.2 Error Budget

Table 2- 7 estimates the error impact and presents some possible mitigation strategies. This section describes potential improvements to mitigate some of these error sources.

Table 2- 7 VOLCAT Error Budget.

Error Source	Magnitude of Retrieval Impacts	Mitigation Strategies
Sensor Noise/Irregular Spectral Effects	0-25%	Occurs infrequently, some mitigation strategies are already in place.
Missing sensor data	0% - 100%	Occurs infrequently. Impact related to level of missing data and which satellite channels impacted. Mitigation strategies are in place, but a minimum number of pertinent channels must be available or the VOLCAT system will exit and not generate products.
Co-registration Errors	0% - 20%	Seldom a concern for a satellite instrument outside of satellite checkout periods. Should such errors be uncorrectable, impact will vary, depending on which channels are impacted and the degree of error.
Calibration Errors	0% - 50%	Seldom a concern for a satellite instrument outside of satellite checkout periods. Most often minor errors will have little to no impact, however more significant calibration errors could have larger impacts.

2.6 Practical Considerations

2.6.1 Numerical Computation Considerations

The VOLCAT application suite is a mixed language application. The bulk of the processing is done using Fortran and C compiled code, as well as python wrappers and helpers. The VOLCAT application suite has been fully containerized and the deployment of the VOLCAT containers are supported with a complete Kubernetes orchestration. The VOLCAT containers and orchestration are hosted on UW/SSEC gitlab and shared with external parties as needed. The complete VOLCAT containers and orchestration come with test cases and automatic verification procedures to ensure numerical accuracy is achieved within machine numerical precision considerations.

2.6.2 Programming and Procedural Considerations

The VOLCAT application suite containers and orchestration allow for rapid deployment with external partners. This process has been exercised with existing research partners and has resulted in stable, repeatable, and easily updated processing capabilities. The VOLCAT application suite Fortran elements are single CPU based (additional CPUs are needed for python and other demands) and consume large amounts of RAM (~15 to as much as 70 GB) per satellite processing stream. Since latency is a significant concern to the aviation community and their requirements, the VOLCAT product latency should be closely monitored and similar latency to the experimental processing system at UW/SSEC should be achieved such that all VOLCAT latency requirements are met.

2.6.3 Quality Assessment and Diagnostics

The VOLCAT product accuracy and requirement assessments described in Section 2.5 should be performed for new satellite sensors to a level of full maturity declaration like what has been accomplished for existing sensors (e.g., GOES-16 ABI, NOAA-21 VIIRS, etc.). These assessments require science team expertise to perform necessary analyses (e.g., cloud advection pattern assessment, manual imagery polygon analysis, etc.).

Additionally, the VOLCAT event files contain quality information that can be used to more automatically monitor system health. The VOLCAT quality information contains categories of optimal pixel percentage, sub-optimal pixel percentage and bad pixel percentage. It should be stressed, the VOLCAT output is event driven—that is the volcanic emissions produced by the Earth in the view each satellite will dictate the frequency and amount of output. It is suggested for automated product health monitoring, long-term averages and standard deviations of pixel categories are computed for each satellite processing stream.

2.6.4 Exception Handling

The VOLCAT application suite will produce log files for the Fortran processing steps and for the python processing steps. The log files will indicate success upon successful completion. The log files will also indicate when errors are encountered with appropriate diagnostic information, where applicable. The log files also contain warnings for non-critical encounters. The VOLCAT application suite is designed to constantly process the latest satellite observations for a given satellite processing stream. Should a failure be encountered, the system is designed to skip the offending observation data and continue with the next (subsequent) satellite observation; otherwise the system latency will grow too large.

2.7 Validation

Section 2.5.3.1 describes how the VOLCAT application suite has been validated. These validation techniques will continue for new satellite sensors in the future and continued monitoring for existing, fully validated satellite sensors.

3 ASSUMPTIONS AND LIMITATIONS

3.1 Performance Assumptions

Section 2.5.3.2 details an error budget for instances when model performance may be significantly degraded.

Some key assumptions:

- The input satellite radiances are well calibrated and without error.
- Characteristics of the input satellite radiances have the same distribution over time (i.e., there is no "drift" in the observations between the training data and real-time data).
- VOLCAT requirements require V&V is performed for cases where volcanic cloud is the highest cloud layer (e.g., volcanic cloud does not have meteorological cloud(s) present between it and the observing satellite).

3.2 Potential Improvements

Future improvements to the VOLCAT application suite are currently being researched via other research funding sources. At present, some of the research that may result in improved VOLCAT performance includes:

- Incorporation of higher resolution information for detection and characterization of volcanic thermal monitoring and improvement of VOLCAT cloud properties (ash height, ash mass loading).
- Utilization of new VOLCAT AI approach to automated volcanic cloud detection. The research currently is focused on improving detection (e.g,. higher probability of detection and lower false alarm rate) using a random forest approach. The research is using a large, expert selected and classified collection of volcanic cases, correct nulls, current VOLCAT false alarms and missed detection. The initial focus is improvement of VIIRS detections; pending success for VIIRS, improvement for other sensors is to be explored should funding be available.
- Additional future research projects that result in VOLCAT improvements will be included in future VOLCAT application suite container and orchestration updates.

4 REFERENCES

Cox, S. K., 1976: Observations of Cloud Infrared Effective Emissivity. *J.Atmos.Sci.,* **33**, 287-289.

Giraud, V., J. C. Buriez, Y. Fouquart, F. Parol, and G. Seze, 1997: Large-scale analysis of cirrus clouds from AVHRR data: Assessment of both a microphysical index and the cloud-top temperature. *J.Appl.Meteorol.,* **36**, 664-675.

Heidinger, A. K. and M. J. Pavolonis, 2009: Nearly 30 years of gazing at cirrus clouds through a split-window. Part I: Methodology. *J.Appl.Meteorol. and Climatology*, **48(6)**, 110-1116.

Inoue, T., 1987: A Cloud Type Classification with Noaa 7 Split-Window Measurements. *J.Geophys.Res.-Atmos.,* **92**, 3991-4000.

Newhall, C.G., and Self, S., 1982, The volcanic explosivity index (VEI): An estimate of explosive magnitude for historical volcanism. Journal of Geophysical Research, v. 87, no. C2, p. 1231–1238, https://doi.org/10.1029/JC087iC02p01231.

Parol, F., J. C. Buriez, G. Brogniez, and Y. Fouquart, 1991: Information-Content of Avhrr Channels 4 and 5 with Respect to the Effective Radius of Cirrus Cloud Particles. *J.Appl.Meteorol.,* **30**, 973-984.

Pavolonis, M. J., W. F. Feltz, A. K. Heidinger, and G. M. Gallina, 2006: A daytime complement to the reverse absorption technique for improved automated detection of volcanic ash. *J.Atmos.Ocean.Technol.,* **23**, 1422-1444.

Pavolonis, M. J., 2010: Advances in Extracting Cloud Composition Information from Spaceborne Infrared Radiances-A Robust Alternative to Brightness Temperatures. Part I: Theory. *Journal of Applied Meteorology and Climatology*, **49**, 1992-2012, doi:10.1175/2010JAMC2433.1 ER.

Pavolonis, M., A. Heidinger, and J. Sieglaff, 2013: Automated retrievals of volcanic ash and dust cloud properties from upwelling infrared measurements*, J. Geophysical Research*, **118(3)**, 1436-1458.

Pavolonis, M., J. Sieglaff, and J. Cintineo (2015a), Spectrally Enhanced Cloud Objects (SECO): A Generalized Framework for Automated Detection of Volcanic Ash and Dust Clouds using Passive Satellite Measurements, Part I: Multispectral Analysis, *Journal Geophysical Research*, **120**, 7813-7841.

Pavolonis, M., J. Sieglaff, and J. Cintineo (2015b) Spectrally Enhanced Cloud Objects (SECO): A Generalized Framework for Automated Detection of Volcanic Ash and Dust Clouds using Passive Satellite Measurements, Part II: Cloud Object Analysis and Global Application, *Journal Geophysical Research*, **120**, 7842-7870.

Pavolonis, M.J., J. Cintineo, and J. Sieglaff, 2018: Automated Detection of Explosive Volcanic Eruptions Using Satellite-derived Cloud Vertical Growth Rates, *Journal Geophysical Research*, **5(2)**, 903-928.

Prata, A. J. and I. F. Grant, 2001: Retrieval of microphysical and morphological properties of volcanic ash plumes from satellite data: Application to Mt Ruapehu, New Zealand. *Q. J. R. Meteorol. Soc.*, **127**, 2153-2179.

Rodgers, C. D., 1976: Retrieval of atmospheric temperature and composition from remote measurements of thermal radiation. *Reviews of Geophysics and Space Physics*, **14**, 609-+.

Van de Hulst, H. C., 1980: *Multiple Light Scattering, Tables, Formulas, and Applications.* Vol. 2. Academic Press, 739 pp.

Wen, S. and W. I. Rose, 1994: Retrieval of sizes and total masses of particles in volcanic ash clouds using AVHRR bands 4 and 5. *J. Geophys. Res.*, **99**, 5421-5431.

Zhang, H., W. P. Menzel, 2002: Improvement in thin cirrus retrievals using an emissivity-adjusted CO2 slicing algorithm. *J.Geophys.Res.-Atmos.,* **107**, 4327, doi:10.1029/2001JD001037.

END OF DOCUMENT